Progress in Additive Manufacturing
https://doi.org/10.1007/s40964-026-01729-1

RESEARCH

Tuning the microstructure and mechanical properties of AlSi10Mg powder bed fusion (PBF-LB) parts by local laser heat treatment

Steffen Kramer[1,2] · Michael Jarwitz[1] · Thomas Graf[1] · Volker Schulze[2] · Frederik Zanger[2]

Received: 13 January 2026 / Accepted: 22 April 2026

Abstract

Laser powder bed fusion (PBF-LB) is increasingly adopted for producing complex aluminum components for lightweight aerospace and automotive applications. However, its broader application is limited by the relatively low fatigue strength of as-built parts. Adjusting the microstructure and mechanical properties of PBF-LB parts to increase their fatigue strength remains a key research focus. Most research concentrates on conventional heat treatment methods which affect the components microstructure globally and are time- and energy-expensive. In contrast, laser heat treatment (LHT) enables to locally tailor the microstructure and mechanical properties efficiently. Still, the potential of LHT for PBF-LB manufactured aluminum components and the underlying mechanisms remain largely unexplored. Therefore, this study investigates the microstructural evolution of PBF-LB manufactured AlSi10Mg parts subjected to a post-PBF-LB LHT. The influence of the key process parameters - laser power, relative movement speed of the laser beam on the part (feed rate), and beam diameter – on the microstructure and hardness – as well as the resulting mechanical properties are evaluated. Hardness, tensile strength, and fatigue performance are compared to the as-built and T6 heat-treated condition. The findings reveal that after LHT the microstructure closely resembles that of conventionally stress-relieved material. The controlled coarsening of silicon particles facilitates dislocation movement, allowing the tuning of hardness and ductility. LHT achieves tensile strengths comparable to T6 heat-treated specimens while offering increased ductility. In the low-cycle fatigue regime (< 1E5 load cycles) LHT specimens achieve the lowest fatigue strength due to the retained heterogenic scan track structure facilitating crack propagation. In the high-cycle fatigue regime (1E5-1E7 load cycles), LHT-treated samples demonstrate improved fatigue strength compared to the as-built condition and equal to T6 treatment owing to a superior defect tolerance. Overall, LHT provides an effective approach for localized microstructural adjustment and tuning of mechanical properties, representing a promising approach to achieve tailored part properties for PBF-LB manufactured parts.

Keywords Laser heat treatment · Powder bed fusion (PBF) · AlSi10Mg · Microstructure · Fatigue · Tensile strength

1 Introduction

Laser powder bed fusion (PBF-LB) allows the manufacturing of lightweight aluminum parts with complex geometries impossible to manufacture with conventional processes like casting or milling. Moreover, aluminum alloy parts manufactured by PBF-LB possess an increased tensile strength and hardness compared to conventionally processed aluminum parts [1, 2] and are increasingly used in applications such as aerospace and automotive [3–5]. The most commonly used aluminum alloy in PBF-LB is AlSi10Mg, which is originally a cast alloy due to its low shrinkage. Numerous studies report a tensile strength of above 400 MPa and a hardness over 125 HV for AlSi10Mg parts manufactured by PBF-LB [6–8] compared to 169–315 MPa and 60–99

✉ Steffen Kramer
steffen.kramer@ifsw.uni-stuttgart.de

Michael Jarwitz
michael.jarwitz@ifsw.uni-stuttgart.de

Thomas Graf
thomas.graf@ifsw.uni-stuttgart.de

Volker Schulze
volker.schulze@kit.edu

Frederik Zanger
frederik.zanger@kit.edu

[1] Institut fuer Strahlwerkzeuge (IFSW), University of Stuttgart, Stuttgart, Germany

[2] wbk Institute of Production Science, Karlsruhe Institute of Technology, Karlsruhe, Germany

Published online: 22 May 2026

HV respectively for gravity-, sand-, or die-cast AlSi10Mg parts [1, 2, 9, 10]. The local heat input by the laser beam as well as high scanning speeds during PBF-LB lead to cooling rates up to 1E5-1E7 K/s [3, 11] resulting in a fine cellular microstructure consisting of supersaturated α-Al surrounded by an Si-rich network with cell sizes around 500 nm [12]. The reasons for the increased strength and hardness in AlSi10Mg PBF-LB parts are the Si-rich cell boundaries, which impede the dislocation movement combined with an increased dislocation density and solid solution strengthening inside the α-Al [13, 14]. The mentioned strengthening mechanisms cause a low ductility and thus a low fatigue strength when compared to cast material [1, 15]. Improving the fatigue behavior of PBF-LB manufactured parts is therefore essential for their application in the critical sectors mentioned before.

Recent studies investigated the effect of conventional heat treatments on the microstructure and mechanical properties of PBF-LB manufactured parts [16]. Numerous studies investigated different heat treatments such as T6 heat treatment, direct aging (DA) or stress relief (SR) heat treatment and their effect on the microstructure with the aim to improve the fatigue properties:

1.1 T6 heat treatment

The T6 heat treatment consists of a solution heat treatment, water quenching and consecutive artificial aging and is commonly used for cast aluminum parts to achieve peak-hardening [17]. The solution heat treatment of PBF-LB manufactured aluminum parts dissolves the heterogenic structure of adjacent scan tracks and layers as well as the fine cellular Si-network and leads to the coalescence of Si particles to form larger, round Si-particles [18]. Additionally, the solution heat treatment triggers the formation of the needle-shaped intermetallic phase β-AlFeSi [19] and reduces the Si-supersaturation of the aluminum matrix [16]. Solution heat treatment starts at a temperature of 400 °C [18] but is mostly carried out at temperatures around 520–535 °C for 1–6 h [20–22]. The following artificial aging treatment is typically carried out at temperatures around 165 °C for up to 48 h and leads to the formation of small (< 10 nm) Mg_2Si-precipitates [19, 23]. The microstructural changes caused by the solution heat treatment reduce the tensile strength and hardness to values around 170–280 MPa and 64–96 HV, respectively [3, 19]. The decrease in strength and hardness correlates with an increasing temperature and hold time [3]. The subsequent precipitation hardening increases hardness and tensile strength of the material significantly. Typical values for tensile strength and hardness of T6 heat-treated PBF-LB manufactured AlSi10Mg are around 292–305 MPa and 100–116 HV, respectively [20, 22, 23]. The loss in strength compared to the as-built condition comes with a significant increase in ductility, which in turn is favorable for the fatigue behavior of PBF-LB AlSi10Mg parts [24]. Numerous studies report an increased fatigue strength for T6 heat-treated AlSi10Mg parts: Aboulkhair et al. [25] measured an increased fatigue strength for T6 heat-treated parts in a rotating bending test as these parts reached the fatigue limit for 3E7 load cycles at a maximum stress of 94 MPa while as-built parts failed prematurely at a lower stress of 63 MPa. This behavior was attributed to the increased ductility as well as to the reduction of residual stress. Di Egidio et al. [26] measured a fatigue strength of 108 MPa for 2E6 load cycles during the rotating bending test. Besides the increased ductility the high fatigue strength was attributed to the homogeneous microstructure as the Si-rich network of the as-built condition was identified as a weak point for crack initiation and crack propagation. Moreover, measurements of the residual stress at the part surface showed residual tensile stress (99 MPa) for the as-built part and compressive stress (-47 MPa) for the T6 heat-treated part. Similar results for the fatigue behavior for T6 heat-treated parts were reported by Mfusi et al. [22] & Di Egidio et al. [27]. In contrast, an experimental investigation by Baek et al. [28] resulted in a 25% decrease in fatigue strength after T6 heat treatment. The reported tensile strength and ductility in the as-built condition were comparable to the results of the before mentioned investigations [22, 25, 26]. However, in the investigation of Baek et al. [28] the T6 heat treatment did not achieve an increase in ductility and the tensile strength dropped to only 241 MPa despite similar heat treatment parameters. The reasons for this discrepancy remain unclear, but are most likely responsible for the surprising decrease in fatigue strength.

1.2 Stress relief heat treatment

Stress relief heat treatment, in literature sometimes also referred to as annealing, is aimed at reducing residual stress inside the part. Especially PBF-LB manufactured aluminum alloy parts possess significant residual tensile stress, which can lead to plastic deformation [29]. SR heat treatment is typically carried out at 250–300 °C for 1–2 h with no subsequent quenching [30, 31]. The elevated temperatures lead to a disintegration of the Si-rich network structure and the formation of spherical Si-particles around the α-Al cells [32]. The Si particle diameter is only 0.08 µm in average compared to 1.8 µm for T6 heat treated material [33]. Additionally, nano-sized Si precipitates form inside the Si-supersaturated α-Al whereas no Mg_2Si precipitates were found [32]. Residual stress at the part surface reduces significantly from 112 to 115 MPa in the as-built condition to 8.7–41.7 MPa after SR [21, 34]. The disintegration of the Si-network

facilitates the movement of dislocations between Al-cells and thus the deformation of the Al-phase [35]. This results in a decrease in hardness (87–92 HV) and tensile strength (250–340 MPa) compared to the as-built condition [21, 31]. The increased ductility of up to 20% elongation at failure however brings maxium toughness compared to the as-built or T6 heat treated material [24]. The fatigue behavior of SR heat treated material is much less researched in comparison to the as-built and T6 condition. Roveda et al. [30] investigated the fatigue crack propagation mechanism for as-built parts as well as two different SR treatments. The results showed a 60–120% increased long crack fatigue threshold. This was mainly attributed to the plasticity-induced crack closure. But further investigations showed no impact on the fatigue strength itself as it is mainly determined by defects [36]. However, investigations by Lehner et al. [21] discovered an increase in fatigue strength following SR treatment. While the fatigue strength of the SR treated material did not reach the level of the T6 heat treated material, it still resulted in a significant improvement compared to the as-built condition. This was attributed to a superior defect tolerance, but a lack of cyclic hardening and lower residual compressive stress compared to the T6 heat-treated material. The discrepancy between the investigations by Roveda et al. [36] and Lehner et al. [21] could be explained by the exceptionally low tensile strength of the specimens used by Roveda et al. in both, the as-built (338 MPa) and stress-relieved (217 MPa) condition. The investigations do not provide any identifiable reason for the low tensile strength.

1.3 Direct aging

DA is performed at 155–180 °C for 2–6 h in a furnace and without subsequent quenching [28, 37]. The procedure is designed for PBF-LB manufactured aluminum parts to achieve maximum hardness and tensile strength [38], which can reach values of up to 153 HV [37] and 450–460 MPa [38, 39]. The low temperature during DA retains the cellular structure and an intact Si-network thereby keeping the strengthening effect of the impeded dislocation movement at the cell boundaries. Slow Si diffusion processes however enable the formation of stable, nano-sized Si-precipitates as well as Mg_2Si precursors inside the Al-phase [40, 41]. The resulting precipitation hardening increases strength and hardness of the material but slightly reduces the ductility [38]. Due to the precipitation of Si inside the Al-phase the supersaturation is reduced which is accompanied by a reduction of the residual tensile stress of the as-built material by 35–50% [26, 38]. Baek et al. measured an increase in fatigue strength of 12.5% compared to as-built specimens and 50% increase compared to T6 heat-treated specimens, which was attributed to the increased tensile strength after direct aging [28]. Di Egidio et al. [26] however reported a 15% decrease in fatigue strength compared to T6 heat-treated specimens, which was presumably caused by a lower resistance to crack initiation due to the intact Si-network of the direct-aged specimens.

This outline of the current research work on heat treatment of AlSi10Mg parts manufactured by PBF-LB clearly demonstrates the effort to adjust microstructure and mechanical properties. But, while microstructural processes during conventional furnace-based heat treatments are well understood, information on the fatigue behavior is limited and at times contradicting. In addition, furnace-based heat treatments are energy-intensive and often time-consuming processes. Conventional heat treatments will remain the most efficient solution for applications such as stress relief heat treatment of largescale, additively manufactured parts and sheet materials. However, conventional heat treatments are always applied to the whole part, which means that also areas of the part are affected for which it could be beneficial to retain the high tensile strength and hardness of the as-built condition. Therefore, to efficiently achieve tailored part properties, approaches for a local adjustment of the microstructure and mechanical properties are desired and researched.

1.4 Local microstructure modification

Current research on the possibilities of local microstructure tailoring of PBF-LB manufactured parts was reviewed by Qi et al. [42]. Evidently, the research on microstructure tailoring is focused on complex in-process approaches such as laser beam shaping or the implementation of auxiliary fields such as magnetic or acoustic fields during PBF-LB. Leis et al. [43] investigated the impact of the cooling rate during PBF-LB on the resulting microstructure and hardness by applying different process parameters. This approach however is limited by the melting and solidifying during PBF-LB. An approach to adjust the parts microstructure post PBF-LB was presented by Noell et al. [44]. The study investigated the impact of electropulsing on the microstructure of PBF-LB manufactured stainless steel parts. While microstructural adaptations were possible, the process also requires a complex infrastructure.

Local laser heat treatment (LHT) allows to constrain the microstructure change to a desired area or part feature and is already well established for the hardening of ferrous parts with high hardness requirements such as pressure die cast tools [45, 46]. The fast heating and cooling of the material surface induces a martensitic transformation of the near-surface microstructure. For aluminum alloys LHT is not yet as widely researched, but multiple studies investigated laser heat treatment of aluminum alloy sheet materials with

Table 1 Material composition of AlSi10Mg powder material in wt-%

Si	Mg	Fe	Mn	Ti	Zn	Cu	Al
9.8	0.35	0.18	0.01	0.03	0.01	< 0.01	Bal.

the aim to increase ductility and formability. First results on the effect of LHT on aluminum alloy sheets were published by Merklein et al. [47]. LHT was applied to the bending edge to increase the maximum bending angles of aluminum sheet and foam materials. Maier et al. [48] later conducted bending experiments on laser heat treated, rolled AA6016 aluminum sheets and showed that the increased formability is due to a recrystallization occurring in the heat affected zone leading to coarse grains and reduced hardness. Pursuing investigations [49] revealed the potential of the LHT process to manufacture aluminum Tailored Heat Treated Blanks or profiles. Similar research by Mohammadi et al. [50] with the aluminum alloy AA2024-T3 showed that LHT also causes a reduction of springback during bending tests. Microstructure and hardness investigations showed that the material experienced annealing as well as partial solution heat treatment during LHT. However, due to the unique microstructural characteristics of PBF-LB manufactured parts, the findings of these studies cannot easily be transferred.

The feasibility of a post-PBF-LB laser heat treatment of PBF-LB manufactured aluminum parts to change the microstructure was only recently shown by Kramer et al. [51]. The LHT process applied significantly reduced the materials hardness by breaking up the Si-rich cellular structure. However, the process mechanism is not well understood as the investigation did not include temperature measurements of the process and did not consider the impact of the LHT on the grain structure. Moreover, the impact of the LHT on the mechanical properties is currently unknown.

Therefore, in this study the possible mechanisms of microstructural change and the corresponding hardness reduction during post-PBF-LB laser heat treatment of AlSi10Mg PBF-LB parts are investigated as well as the influence of laser power, feed rate and beam diameter on these microstructural and hardness changes. The role of the part geometry is also considered. Eventually, tensile and fatigue strength of as-built, laser heat-treated and T6 heat-treated specimens are measured to assess and compare the impact of the LHT process on the mechanical properties.

2 Materials & methods

The AlSi10Mg powder material for specimen production with a size distribution of 20–63 µm was supplied by m4p material solutions GmbH (Magdeburg, Germany). The chemical composition is given in Table 1.

Table 2 PBF-LB process parameters for the specimen production

Parameter	Hatching	Contour
Laser power	350 W	250 W
Scanning speed	1150 mm/s	555 mm/s
Hatch distance	170 µm	–
Layer thickness	50 µm	50 µm

Specimens were manufactured on a SLM 280HL machine from Nikon SLM Solutions GmbH using a fiber laser with a wavelength of 1070 nm and a maximum power of 400 W. The beam profile of the laser beam after the focusing optics was measured according to DIN EN ISO 11146–2. The focus diameter was 83 µm, the Rayleigh length was 3.77 mm and the M^2 was 1.33. All specimens were manufactured using the process parameters recommended by the machine supplier, listed in Table 2.

For the volume ("hatching") of the part a conventional stripe pattern with a 67° rotation between every layer was used. A second parameter set ("contour") was used to manufacture the outer layer of the parts and ensure a satisfactory surface quality. The build chamber was flooded with Argon to create an inert atmosphere. To reduce residual stresses inside the part during the manufacturing process the build platform on which the specimens were manufactured was heated to 100 °C. The given parameters resulted in a relative part density of > 99.7%. Specimens were manufactured in an upright orientation with a length of 50 mm, a width of 30 mm and a thickness of 2 mm. Specimen geometry and process strategy are depicted in Fig. 1. All specimens were cut from the build plate using electric discharge machining and cleaned with water and ethanol prior to laser heat treatment.

The laser heat treatment was performed with an Yb:YAG thin-disk laser (TruDisk 8001, Trumpf, Ditzingen/Germany) with a wavelength of 1030 nm. The laser beam after the focusing optics was measured to have an M^2 of 17.5 and a Rayleigh length of 9.7 mm. The beam diameter on the specimen surface desired for the laser heat treatment was obtained by shifting the focusing optics in z-direction. The focusing optics was tilted by 5 degrees from normal incidence to avoid any issues with reflecting laser radiation. Specimens were fixed in a clamping device, which was isolated with a layer of rough sandpaper to limit heat loss. Laser heat treatment was performed by moving the clamped specimen under the laser beam as depicted in Fig. 2. The laser was switched on immediately before the specimen entered into the beam and switched off when the beam left the rear end of the specimen, thereby heat-treating the entire

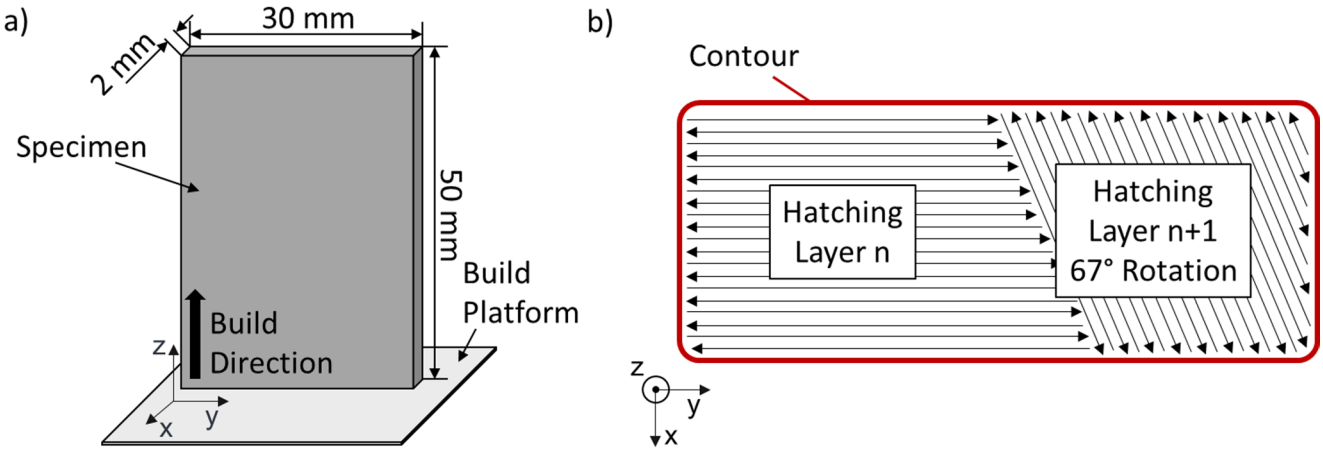

Fig. 1 **a** Schematic depiction of the specimen geometry and the process setup for the specimen manufacturing. **b** Schematic depiction of the applied scanning strategy

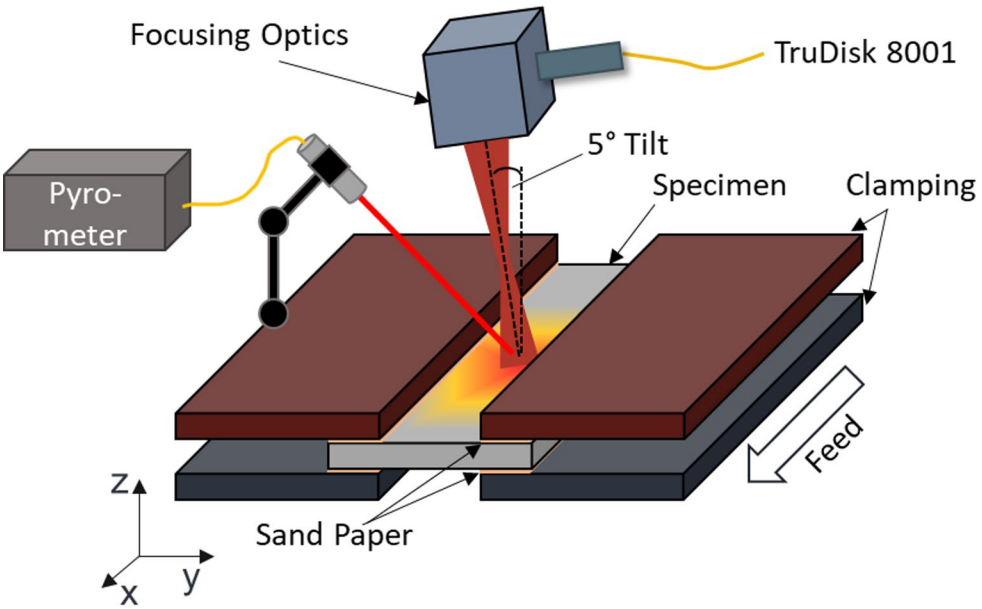

Fig. 2 Experimental setup for laser heat treatment

length of the specimen. During the experiments the process parameters laser power (320–500 W), relative movement speed of the laser beam on the specimen ("feed rate", 0.15–0.25 m/min) and beam diameter on the specimen surface (3.3–10 mm) were varied. Details on all tested process parameter sets are given in Appendix A1. The temperature was measured at a fixed position on the specimen surface in the middle of the specimen with a one-color pyrometer (Mergenthaler, Germany). The measurement spot of the pyrometer was 2.5 mm in diameter on the specimen surface and the emission coefficient was set to 0.45 [52]. The calculated minimum measurable temperature after calibration is given with 190 °C but is superimposed with heavy noise at such low temperatures. Therefore, only temperature date exceeding 200 °C was considered valid.

The laser heat-treated specimens were cut in the middle, perpendicular to the feed direction, and the resulting cross-sections were prepared for metallographic investigation with embedding, grinding and polishing. Hardness was measured 1 mm below the sample surface along the cross-section to investigate local hardness variations, using an ATM Carat 930 (ATM, Germany) hardness tester with a testing force of 0.98 N. Measurements were averaged over at least four cross-sections taken from two identical specimens. Microstructural investigations as well as investigations of pores and scan track morphology were carried out with optical microscopy (Leica, Germany) and scanning electron microscopy (SEM; JSM-6490LV, Jeol, Japan). For this, the cross-section surfaces were finished with vibratory polishing and etched with Barker's etchant. The grain structure was investigated with Electron Backscatter Diffraction

(EBSD) using an Auriga SEM (Zeiss, Germany) equipped with an EBSD detector (EDAX, USA).

Tensile and fatigue tests were carried out for one representative LHT parameter set, selected based on the results from the microstructure and hardness investigations. Specimens underwent laser heat treatment from both sides with alternating feed directions and a cool down to room temperature between the two processing steps. In this way all possible impacts of microstructure gradients from the LHT over the thickness of the specimen or along the feed direction on the results of the mechanical testing could be avoided. The specimen geometries for the tensile and fatigue tests were cut from the center of the PBF-LB manufactured specimens with laser cutting. For tensile testing the "dog-bone" shaped specimen geometry given in DIN EN ISO 50125 was scaled down to a length of 45 mm. Fatigue specimens were rectangularly shaped with a size of 45 × 20 × 2 mm³. As-built specimens and T6 heat-treated specimens from the same batch were used as reference. The T6 heat treatment consisted of a solution annealing at 525 °C for 6 h, quenching in water and a subsequent artificial aging at 165 °C for 7 h as in [17]. All surfaces of mechanical testing specimens were polished after laser cutting with a semi-automatic polishing machine and a sandpaper with a grit of P1000 to guarantee comparable surface conditions and prevent an impact of the surface quality on the measurement results. Tensile tests were performed according to DIN EN ISO 50125 with the aim to investigate the impact of the laser heat treatment on the ultimate tensile strength (UTS). Fatigue tests were performed using the three-point bending method and a stress ratio of R = -1. The pearl string method according to DIN EN ISO 50100 was applied to estimate the S-N curve in the high-cycle fatigue region between 1E4 and 1E6 load cycles with a failure probability of 50%. The residual stress at the polished surface of the fatigue specimens was measured with X-ray diffraction (XRD) according to EN 15305 using the DR45 XRD measurement device (Stresstech, Germany). The penetration depth of the radiation, at which the intensity value decreased to 1/e of the initial intensity, with the used setup is approximately 11.5 µm. Residual stress measurements were performed with Cr-Kα radiation and a voltage of 30 kV for 30 s, using the modified χ measurement method to increase measurement accuracy.

3 Results and discussion

First the resulting hardness profiles after LHT with different process parameters are presented together with the corresponding pyrometric temperature measurements. Following, the changes in microstructure and the underlying mechanisms are discussed. Furthermore, the tensile and fatigue properties of as-built, laser heat-treated and T6 heat-treated material are compared and discussed in relation to their respective microstructure and residual stress condition.

3.1 Investigation of hardness and microstructure

In a first step the range of achievable hardness values and resulting microstructures were investigated by a systematic variation of the LHT process parameters laser power, feed rate and beam diameter. For this, every process parameter was varied while keeping the remaining two parameters constant (cf. Appendix A1). The results of the hardness measurements are summarized in Fig. 3.

For all investigated combinations of the process parameters, a reduction of hardness compared to the hardness in the as-built condition was observed. The resulting hardness after LHT covers the complete range between as-built (125.6 HV) and a minimum of 82 HV, which was achieved with a laser power of 500 W, feed rate of 0.25 m/min and a beam diameter of 7.5 mm (see Fig. 3a, purple line). The results in Fig. 3a&b further show, that the resulting hardness decreases with an increasing heat input, achieved either by increasing the laser power or by reducing the feed rate. All measured hardness profiles show little to no distinct

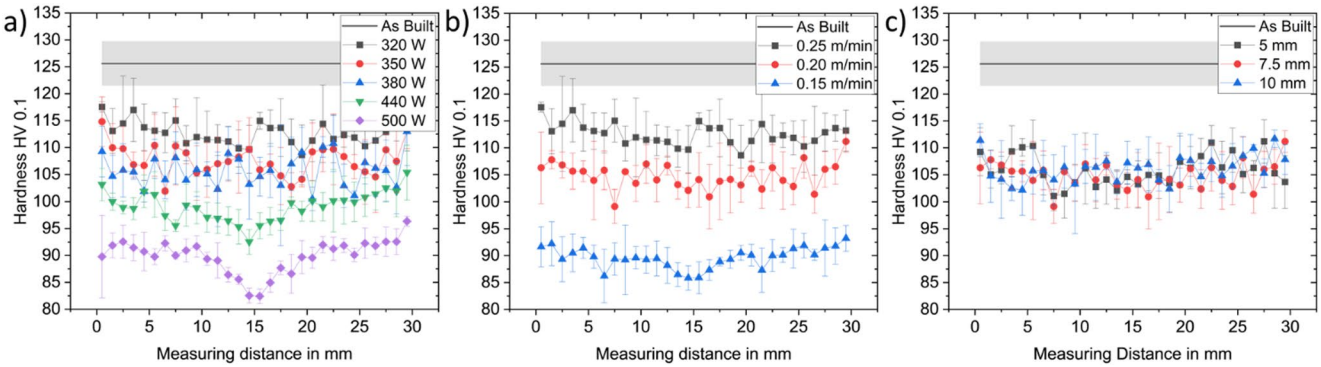

Fig. 3 Hardness measurements perpendicular to the LHT feed direction for different laser heat treatment process parameters. **a** Laser power variation (v = 0.25 m/min, d = 7.5 mm), **b** Feed rate variation (P = 320 W, d = 7.5 mm), **c** Variation of the beam diameter (P = 320 W, v = 0.20 m/min)

local drop in hardness, e.g., in the middle of the specimen where the laser beam was incident on the specimen surface. Instead, the measured hardness is rather homogeneous along the width of the specimens. This indicates an almost homogeneous heating and cooling process perpendicular to the feed direction for the given experimental setup. Reason for that could be the superior heat conduction of aluminum and the applied thermal isolation of the specimens. First of which ensures a quick, homogeneous heat distribution inside the specimen and the second prevents the formation of steep temperature gradients as it reduces the heat flow out of the specimen. This also holds true for the different beam diameters used, as shown in Fig. 3c. The presented results demonstrate, that the resulting hardness is greatly determined by the overall heat input, which is constant for all hardness profiles in Fig. 3c.

A weighted multiple linear regression is performed, to quantify the individual impact of the process parameters on the resulting hardness as well as to check for relevant interdependencies between two parameters. The complete list of all eighteen parameter combinations which were tested and utilized for the regression analysis is given in Appendix A1. The regression equation for the hardness H was set up with mean-centered parameters. The full model as well as the detailed results of the regression are given in Appendix A2. The resulting regression equation with all statistically significant terms ($p \leq 0.1$, $R^2 = 0.94$, adj. $R^2 = 0{,}90$) is given in Eq. 1:

$$\begin{aligned} H =& 110.61\,\mathrm{HV} - 0.13\frac{\mathrm{HV}}{\mathrm{W}}\left(P - \bar{P}\right) \\ &+ 196.24\frac{\mathrm{HV}}{\frac{\mathrm{m}}{\mathrm{min}}}\left(v - \bar{v}\right) \\ &+ 22{,}26\frac{\mathrm{HV}}{\frac{\mathrm{m}}{\mathrm{min}}\cdot\mathrm{mm}}\left(v - \bar{v}\right)\left(d - \bar{d}\right) \end{aligned} \tag{1}$$

The regression analysis confirms that the hardness is primarily governed by the laser power P and feed rate v. The beam diameter d has no significant impact on the resulting hardness. A minor significant interdependency is found for v and d, which corresponds to the area irradiated per unit time.

To assess the underlying mechanisms for the hardness reduction caused by the LHT, the resulting temperature profiles and microstructures were investigated in the middle of the specimens at the exact position where the temperature measurement was carried out. This allows a combined and comprehensive consideration of hardness, microstructure and temperature data in order to explain the microstructural mechanisms during LHT. Figure 4 shows exemplary temperature profiles related to the hardness measurements presented in Fig. 3. All temperature profiles include two distinct peaks. The first peak is the maximum temperature and correlates to the moment at which the laser beam overlaps the pyrometer's measurement spot. The second peak is caused by heat accumulating at the rim of the specimen in the moment at which the laser beam moves towards the rim of the specimen. Figure 4a&b demonstrate the increase in heat input with increasing laser power and decreasing feed rate, resulting in a higher peak temperature and an extended duration of temperatures above 200 °C. Pyrometer measurements of the parameter set with maximum laser power (Fig. 4a, purple line) reveal a maximum temperature of 557 °C in the pyrometer's measurement spot, which is close to the melting point of AlSi10Mg, which according to literature is 577 °C [8]. As melting of the part should be avoided, it is believed, that the corresponding hardness of 82 HV represents the limits of hardness reduction by LHT. Figure 4c shows that the variation of the beam diameter has only a minor influence on the resulting temperature profiles which are nearly identical and are mainly influenced by the overall heat input. The change in beam diameter only influences the peak temperature. In the following the changes in microstructure are presented and discussed based on the

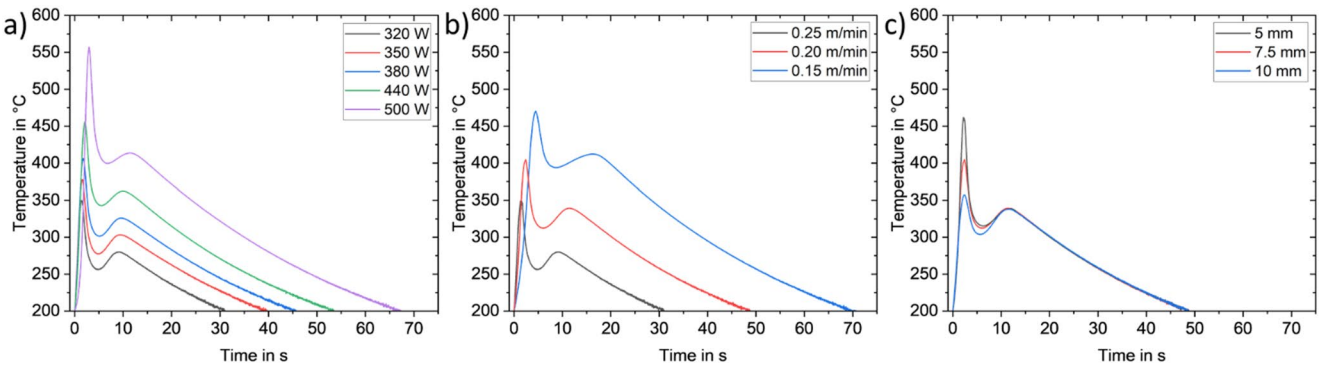

Fig. 4 Exemplary Temperature measurements from the center of the specimen acquired with a pyrometer. **a** Laser power variation (0.25 m/min, 7.5 mm), **b** Feed rate variation (320 W, 7.5 mm), **c** Variation of the beam diameter (320 W, 0.20 m/min)

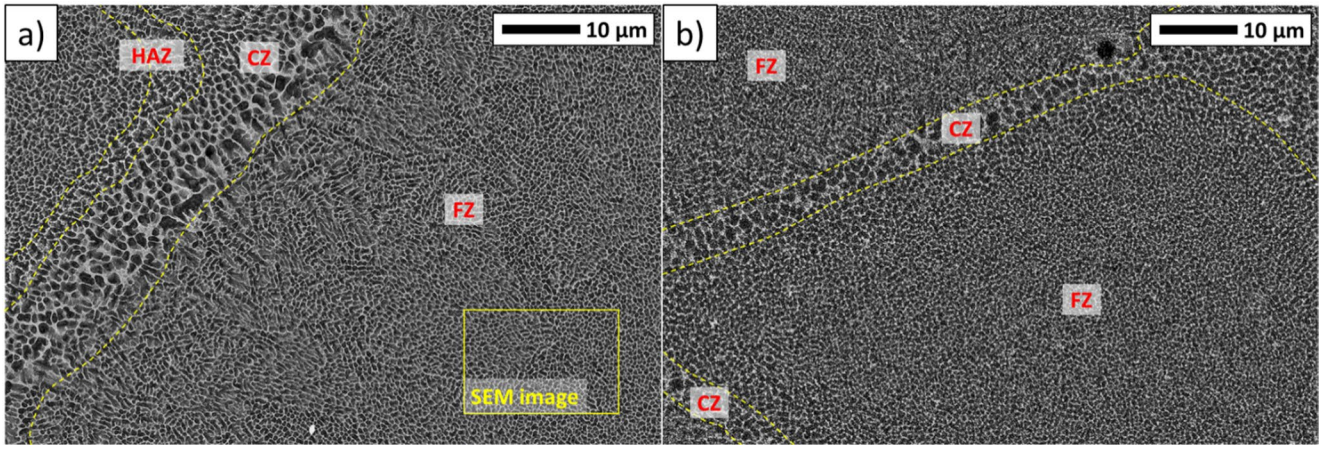

Fig. 5 **a** SEM image of the different melt pool regions from the PBF-LB process and their distinctive microstructure in the as-built condition. (FZ: fine zone, CZ: Coarse Zone, HAZ: heat affected zone). Representative location of the SEM images for investigation of the microstructure highlighted with a yellow rectangle. **b** SEM image of the fine and coarse zone after LHT (LHT process parameters: 500 W, 0.15 m/min, 7.5 mm)

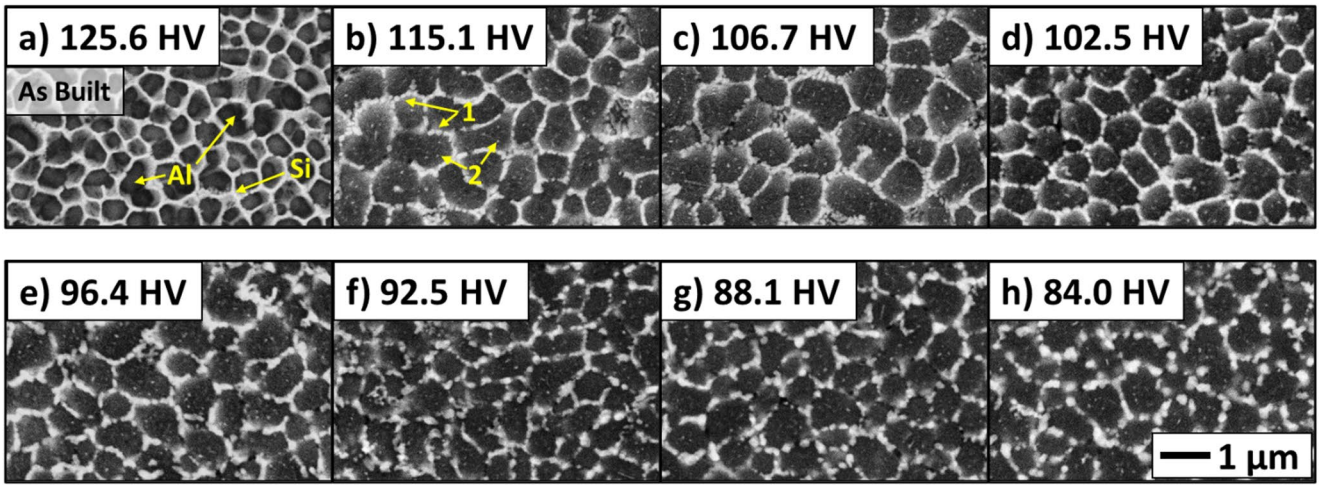

Fig. 6 Representative SEM images from the center of different laser heat-treated specimens showcasing the change in microstructure with the corresponding material hardness. The given hardness values represent the average value of all indentations in the area covered by the pyrometer's measurement spot. (**a**) As-Built, (**b**) 320 W, 0.25 m/min, 7.5 mm, (**c**) 380 W, 0.25 m/min, 7.5 mm, (**d**) 320 W, 0.20 m/min, 5 mm, (**e**) 440 W, 0.25 m/min, 7.5 mm, (**f**) 350 W, 0.20 m/min, 7.5 mm, (**g**) 320 W, 0.25 m/min, 7.5 mm, (**h**) 500 W, 0.15 m/min, 7.5 mm

SEM investigations. The microstructure of PBF-LB parts is usually heterogeneous in the as-built condition, due to the local melting of powder material and remelting of the part surrounding the scan track during PBF-LB. It is defined by a cellular network (see Figs. 5a and 6a) consisting of a Si-rich phase (light grey in SEM image) which surrounds an α-Al phase (dark grey in SEM image). The center of the solidified melt pool consists of a fine cellular structure hereafter called the fine zone (FZ). At the rim of the solidified melt pool the cellular structure is coarse (coarse zone: CZ) and irregular. The solidified melt pool is surrounded by a heat affected zone (HAZ), which is characterized by a fine but broken cellular structure. Since the heterogenous structure consisting of coarse and fine zone is retained after the LHT (see Fig. 5b) [51] and the FZ accounts for the majority of the part volume and provides the most reproducible results, all further SEM images are taken from the FZ, as highlighted in Fig. 5a. Due to the microstructural changes during LHT the HAZ and FZ are not distinguishable anymore (see Fig. 5b).

Figure 6 shows representative SEM images of the microstructure in the as-built condition (Fig. 6a) and seven different LHT parameter sets with steadily increasing heat input and decreasing hardness (Fig. 6b-h). A complete list of all tested parameter sets and resulting hardness values is given in Appendix A1. The SEM images allow the observation of two separate changes in microstructure, indicated with the following numbers in Fig. 6:

(1) The breaking of the Si-rich network and agglomeration of near-spherical Si particles along the former cellular structure.
(2) The precipitation of small Si-particles inside the α-Al phase.

In general, a progressing disintegration of the Si-rich network and agglomeration of Si-particles can be observed with decreasing hardness. The Si-rich network in the as-built condition represents the eutectic phase of the Al-Si alloy and possesses a lamellar structure. Due to the severe undercooling and quick solidification during the PBF-LB process Si is captured in the α-Al which leads to a Si-supersaturation [3]. The heating of the material during LHT enables Si diffusion processes, which are also known from conventional heat treatments of PBF-LB manufactured and cast Al-Si alloy parts [26, 40, 41]. The Si diffusion breaks up the lamellar structure of the eutectic phase and leads to the agglomeration of Si along this former structure, eventually producing pure Si particles. Figure 6 demonstrates that the agglomeration of Si is a continuing process, as Si particles increase in size with decreasing hardness and increasing heat input during LHT. The conversion of the Si-rich network structure to lined up Si particles causes the disintegration of the network. Opposed to the modification of the Si-rich network, the precipitation of Si-particles is not a continuing process. Small precipitations inside the α-Al phase already appear at comparatively low heat inputs, leading to a slight hardness reduction (Fig. 6b) and remain unchanged for higher hardness reductions and heat inputs (Fig. 6c-h). This behavior can be explained by the Si supersaturation of the α-Al phase presumably leading to very short diffusion distances necessary for Si atoms to form precipitations. The observed behavior suggests, that already for a low heat input the formation of the Si precipitations is concluded and the Si supersaturation is degraded.

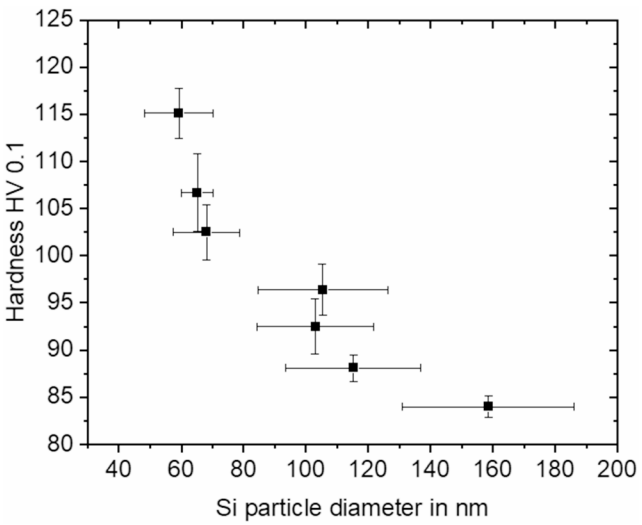

Fig. 7 Relation of the Si-particle diameter and the resulting hardness of the microstructure

To quantify the correlation between microstructural changes and mechanical properties, the average diameter of Si-particles was evaluated for every SEM-image in Fig. 6. For the evaluation only Si-particles originating from the eutectic phase at the cell boundaries are taken into account. Si-precipitations inside the α-Al phase are not considered, as the formation of these precipitations is already concluded at a low heat input. The measured hardness over the evaluated average Si-particle diameter is given in Fig. 7. The results show a steep decrease in hardness for small Si particle diameters. This sudden loss in hardness is most likely not linked to the particle diameter itself but can be attributed to the breaking of the cellular structure. This leads to a loss of the strengthening effect formerly evoked by the impeded dislocation movement at the cell boundaries. The continued, slower loss in hardness for larger particle diameters is most likely caused by a reduced precipitation hardening effect due to the increasing size of the particles leading to dislocations bypassing the particles [53] rather than accumulating at the particles

Similar changes in microstructure and hardness as presented in Fig. 6f-h have been reported in literature for conventional stress relief heat treatments of PBF-LB AlSi10Mg parts. Padovano et al. [24] achieved a comparable microstructure as in Fig. 6g&h after a SR heat treatment at 300°C for 2 h, which resulted in a hardness of 85.6–91 HV. The Si-particle size is given with 100–300 nm, which correlates well with the observed particles in the SEM images in Fig. 6h. Hwang et al. [34] performed SR heat treatment at 280°C for 2 h, observed the same microstructural developments and measured a hardness of 90 HV. The temperature during LHT of the specimen in Fig. 6h is given in Fig. 4a (purple line). The maximum measured temperature exceeded 550 °C for a short time and stayed over 300°C for around 35 s. While the maximum temperature clearly exceeds the starting temperature for solution heat treatment of 400°C given by Cabrini et al. [18], no microstructural changes typical for solution heat treatment can be observed in the SEM images in Fig. 6. The size of the Si-particles is one order of magnitude too small and there are no signs of particles of intermetallic phases such as β-AlFeSi as described in Sect. 1. Ogris et al. [54] conclusively described the spheroidization of Si in Al as interdiffusion of Si atoms in aluminum. The diffusion coefficient

$$D = D_0 \cdot \exp\left(-\frac{Q_{inter} - Q_{vac}}{R \cdot T}\right) \quad (2)$$

with the pre-exponential factor D_0, the activation energy for interdiffusion Q_{inter}, the activation energy for vacancy

formation Q_{vac}, the temperature T and the universal gas constant R, describes the speed of the diffusion process. With the, for the Al-Si alloy A356 provided, pre-exponential factor D_0 = 2.29E-4 m²/s, an activation energy of 148.6 kJ/mol for interdiffusion and an activation energy of 74.3 kJ/mol for vacancy formation [54], the diffusion coefficient during SR (300 °C/2 h) is 3.9E-11 m²/s while the maximum diffusion coefficient during LHT (557 °C) is 4.8E-9 m²/s. It is therefore concluded, that while the duration of the LHT is much shorter compared to a conventional SR heat treatment, the higher diffusion coefficient during LHT enables faster diffusion processes. Tang et al. [38] proposed that a parallel Si diffusion through dislocations and vacancies, called short-circuit diffusion, could be involved in the formation of Si-precipitations. Due to a reduced activation energy compared to interdiffusion the short-circuit diffusion could contribute significantly to microstructural changes, especially at low temperatures. Therefore, the short-circuit diffusion could be responsible for the precipitation of nano-sized Si particles during LHT, even at comparably low temperatures and short heating times, as observed in Fig. 4a (black & blue line), corresponding to the microstructure in Fig. 6b&c. Despite the higher maximum diffusion coefficient during LHT, the duration of the process does not seem to be sufficient for the formation of a microstructure typical for solution heat treatment or T6 heat treatment with artificial aging.

The impact of the part geometry and heat dissipation conditions on the resulting hardness after LHT were investigated using two alternative experimental setups. While the "standard" setup is shown in Fig. 2, LHT was also performed on 90° rotated specimens thereby moving the laser beam perpendicular to the build direction. As the thickness of the specimen is small compared to its width and the diameter of the laser beam, quasi two-dimensional heat conduction can be assumed for the slow feed rates investigated, with the main direction of the heat flow being towards the sides. By rotating the specimen by 90°, and thereby increasing the thermal mass lateral to the feed direction, more heat can be dissipated towards the side compared to the original setup. Further, by rotating the specimen, the length of the laser beam path on the specimen shortens and thereby the total amount of energy induced into the specimen reduces. The second alternative setup was achieved by keeping the feed direction parallel to the build direction but removing the sand paper isolation from the clamping. With this setup the heat flow to the sides of the specimen is also increased as heat now dissipates into the clamping device. In this setup however, the length of the laser beam path on the sample is kept constant. LHT experiments with the alternative setups were performed with one exemplary parameter set (laser power: 500 W, feed rate: 0.25 m/min, beam diameter: 7.5 mm). Temperature and hardness measurements for the different setups are shown in Fig. 8.

Both alternative setups lead to a reduction of the maximum temperature and to a faster cooling at the pyrometer measurement spot, resulting in a reduction of the duration where the temperature exceeds 200 °C. It is therefore concluded, that both alternative setups lead to significantly steeper temperature gradients inside the specimen. As it is shown in Fig. 8b, the hardness drops down to 90–100 HV only in the center which was directly irradiated by the laser while further towards the sides the hardness remains at the as-built level. This shows that it is also possible to restrict the LHT to a defined area and that the effect of LHT strongly depends on the heat dissipation conditions, and therefore, part geometry plays import role.

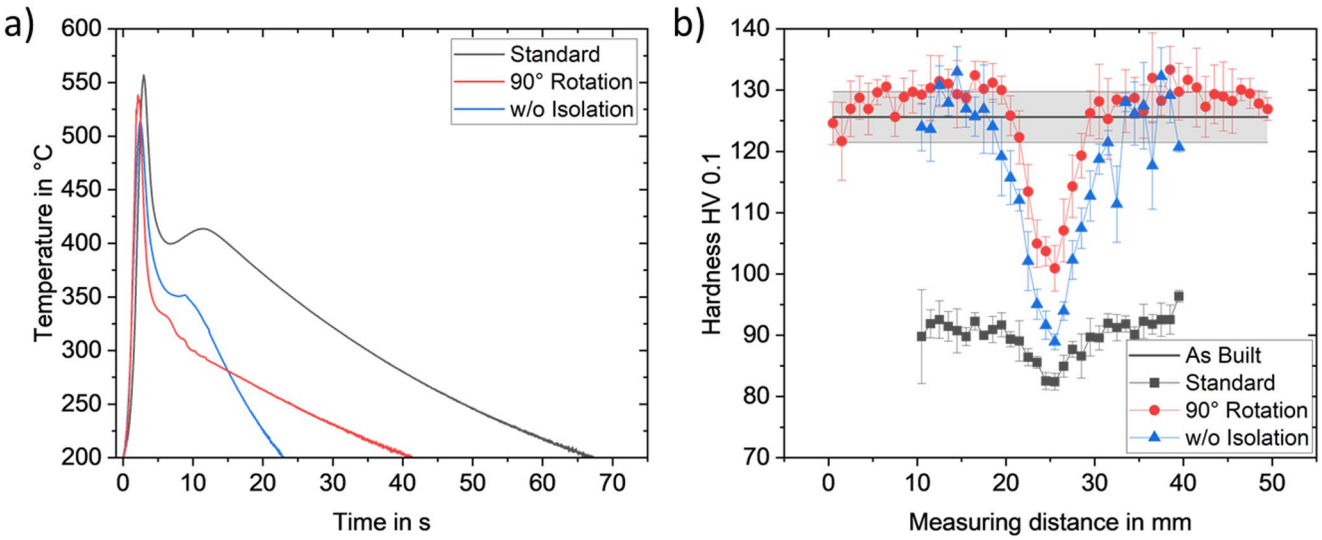

Fig. 8 Temperature and hardness measurements for alternative experimental setups: Rotation of the specimen by 90° & LHT without (w/o) sand paper isolation. All experiments conducted with 500 W, 0.25 m/min and 7.5 mm beam diameter

In the following the depth effect of the LHT is evaluated on the experiments in standard setup and in the setup without isolation presented in Fig. 8. For this, hardness was additionally measured near the top and bottom surface of the polished cross-sections. A distance of 300 µm to the surface was chosen for the measurement to avoid hardness measurements in the contour region (see Fig. 1) because the different PBF-LB process parameters used for contour scanning could influence the hardness [55]. Comparing the hardness measurements from the top, middle and bottom of the specimen as presented in Fig. 9 shows only minor differences in hardness. While the hardness is lowest at the top and highest at the bottom of the specimen for both experimental setups, this effect is hardly significant considering the standard deviation of the measurements. This supports the assumption that the microstructural and hardness changes reported in this section are representative for the entire thickness of the samples and therefore also for the results of the mechanical investigations presented in the following.

3.2 Microstructure of specimens for mechanical testing

Tensile and fatigue tests were carried out with samples in the as-built, T6 heat-treated, and laser heat-treated condition to investigate the impact of LHT on the mechanical properties in comparison to the two most commonly used conditions. One representative set of LHT process parameters was chosen to ensure a significant hardness reduction and change in microstructure: laser power: 320 W, feed rate: 0.15 m/min and beam diameter: 10 mm. The large beam diameter of

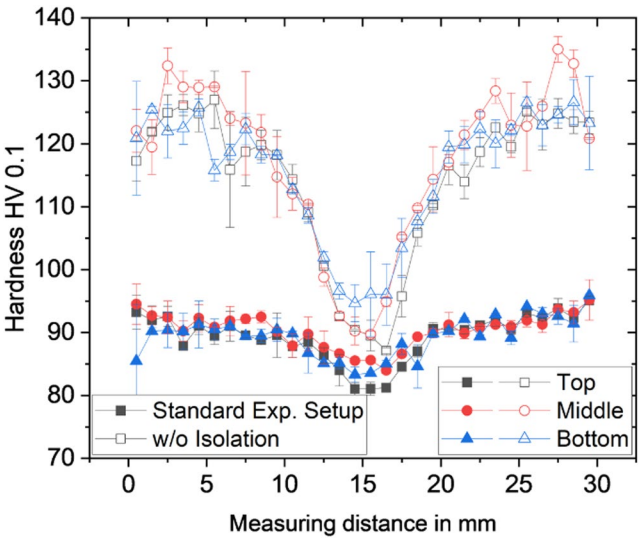

Fig. 9 Hardness measurements for the investigation of the depth effect of the LHT process. Hardness was measured in the middle and 300 µm from the top and bottom surface of the specimens to avoid the contour region of the part. Laser power: 500 W, feed rate: 0.25 m/min, beam diameter: 7.5 mm

10 mm was chosen to ensure a homogeneous modification of the microstructure and thereby homogeneous mechanical properties over the cross-section of the testing specimens. Prior to mechanical testing, the macro- and microstructure of the specimen material was investigated. Optical microscope and SEM images of the specimen material are presented in Fig. 10.

The macroscopic image of the as-built specimen (see Fig. 10a) shows the typical structure of overlapping scan tracks and the contour region with horizontal scan paths at the top and bottom of the image. The scan track structure is retained by the LHT process (Fig. 10b) but is dissolved by the T6 heat treatment (Fig. 10c). The T6 heat treatment leads to the formation of small pores along the scan track borders but also larger pores which lead to delamination between the contour layer and the part volume. The formation of pores is associated with the agglomeration of excessive hydrogen as already found by Girelli et al. [56]. SEM images of the scan track border (Fig. 10d&e) show the typical coarse microstructure at the border for as-built and LHT specimens. Close-up images reveal the typical cellular network structure in the as-built condition (Fig. 10g), which is broken up by the LHT process (Fig. 10h). The microstructure of the T6 specimens comprises of an Al-phase with near-spherical Si-particles evenly distributed and needle-like precipitations of an Fe-rich intermetallic phase which is known to be the β-AlFeSi phase (Fig. 10i) [19]. The inverse pole figure mappings of the grain structure obtained by EBSD (see Fig. 10j-l), show the typical grain orientation of PBF-LB manufactured parts with grains at the rim of the melt pool growing towards the center of the melt pool (101-direction) and grains at the center growing in build direction (001-direction). This grain morphology is maintained even after LHT and T6 heat treatment. Investigations by Sajadi et al. [23] and Ghio et al. [57] concluded, that the grain size and orientation is not affected by conventional heat treatments while Takata et al. [33] and Valim et al. [37] measured a slight grain coarsening, especially at the scan track borders, after T6, DA or SR heat treatment. The increase in grain size however is well within the measurement fault tolerance [16]. On that basis, grain coarsening during LHT is deemed highly unlikely.

3.3 Mechanical investigations

The three different materials were tested in a quasi-static tensile testing setup. Due to the comparatively small size of the specimens, an exact measurement of the elongation with an extensometer was not viable. Therefore, as an approximation, the ductility of the material was assessed by comparing the cross-sectional area before and after the tensile tests and calculating the corresponding reduction of area

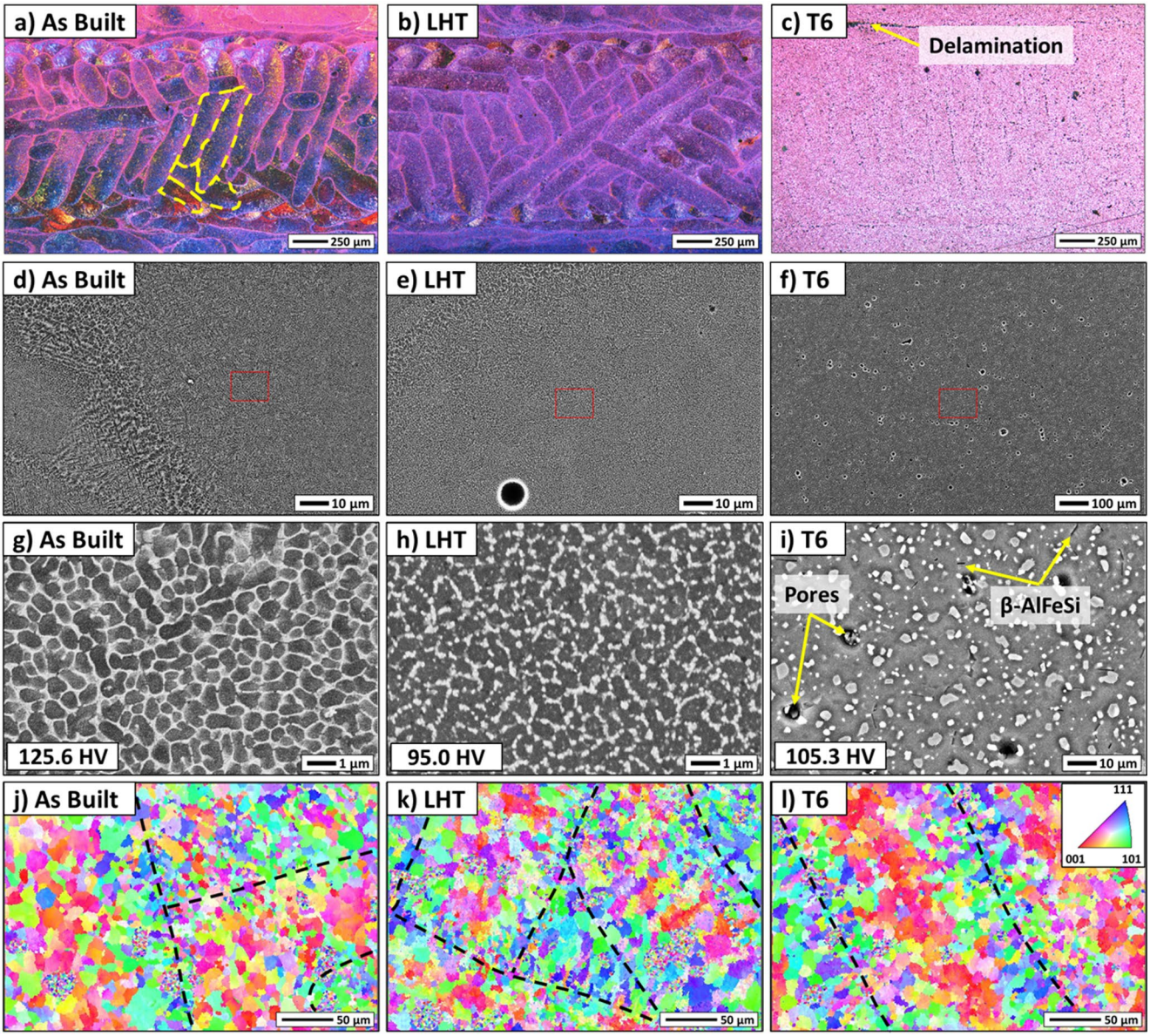

Fig. 10 **a-i** Macroscopic and microstructure images of the tested specimen material. LHT was performed with 320 W, 0.15 m/min and a beam diameter of 10 mm. T6 heat treatment consisted of a solution heat treatment (6 h at 525 °C) subsequent quenching in water and artificial aging (7 h at 165 °C). **j-l** EBSD images of the grain structure. Single scan track borders are highlighted with a dashed line

caused by necking. Results of the tensile tests are presented in Fig. 11.

The UTS of the as-built material is 422 MPa which is in good agreement with results from literature [8]. The T6 heat treatment causes the UTS to drop to 254 MPa. This is caused by the dissolution of the Si-rich network structure and the resulting loss of grain boundary strengthening. Dislocations in the material can now move easily through the material giving the material an increase in ductility. The precipitation hardening effect of Si-particles and intermetallic phases does not compensate for this loss in strength [35]. The measured UTS is slightly below the values reported in **Sect. 1.** This can be attributed to the smaller specimen geometry, as the size of the pores relative to the specimen is larger and therefore stronger affects the mechanical properties. The UTS of the laser heat treated specimens is 273 MPa. The reduction in strength compared to the as-built condition is caused by the breakup of the Si-rich network. The smaller size of Si-particles compared to the T6 specimens contribute to a higher strength while absence of intermetallic phases and pores increases the ductility. Li et al. [35] reported a similar drop in strength for a stress-relieved specimen with similar microstructure as the LHT specimen. It was reasoned that the drop is caused by the partial-cellular

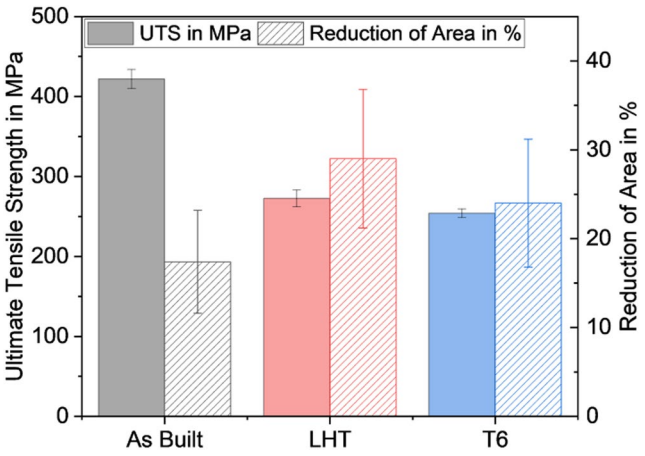

Fig. 11 Ultimate tensile strength (UTS) and reduction of area for as-built, laser heat-treated (LHT) and T6 heat-treated specimens. The reduction of area describes the change in cross-sectional area due to necking during the tensile tests

structure which allows dislocations to move through the Al-phase and therefore does not constrain the deformation of the Al-phase.

In the following the impact of these microstructural changes on the fracture mechanics is discussed, based on optical microscope and SEM images of polished cross-sections of the fractured specimens, as presented in Fig. 12. All fracture surfaces show an inclined fracture pattern with the crack propagation orientated diagonally to the direction of the principal stress (see Fig. 12a, d&g). All fractures can therefore be identified as shear failure which is typical for ductile materials. Necking is most prominent for the LHT specimens. The fracture of the as-built specimen mostly follows the scan track borders as highlighted by the arrows in Fig. 12b. This behavior has also been reported by [58], consequently identifying the CZ at the scan track borders as a weak point of the microstructure. For the LHT specimens the fracture does not follow the CZ but crosses diagonally through single scan tracks (see Fig. 12e). The SEM images reveal that for the as-built specimen the fracture consequently follows the Si-rich network, as highlighted in Fig. 12c, resulting in a smooth fracture surface. Due to the breakup of the Si-rich network during the LHT process, the fracture cannot follow the network structure. The SEM investigation shows a dimple fracture with a rough fracture surface (see Fig. 12f). This is caused by the facilitated deformation of the Al-phase. The fracture behavior is therefore significantly more ductile and results in a higher energy

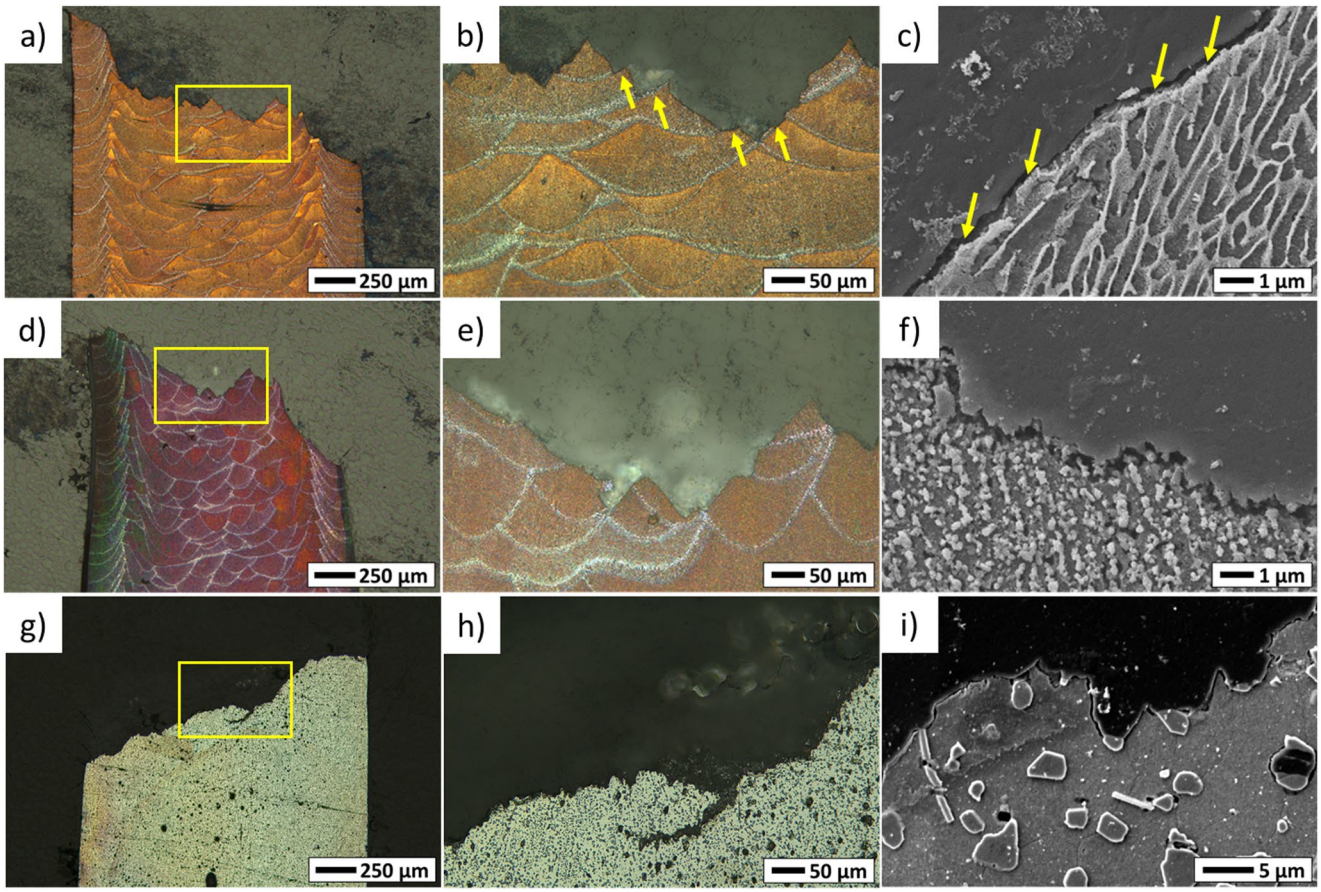

Fig. 12 OM and SEM images of the fracture profiles for the tested materials. (**a**)-(**c**) As-built, (**d**)-(**f**) LHT, (**g**)-(**i**) T6 heat treated

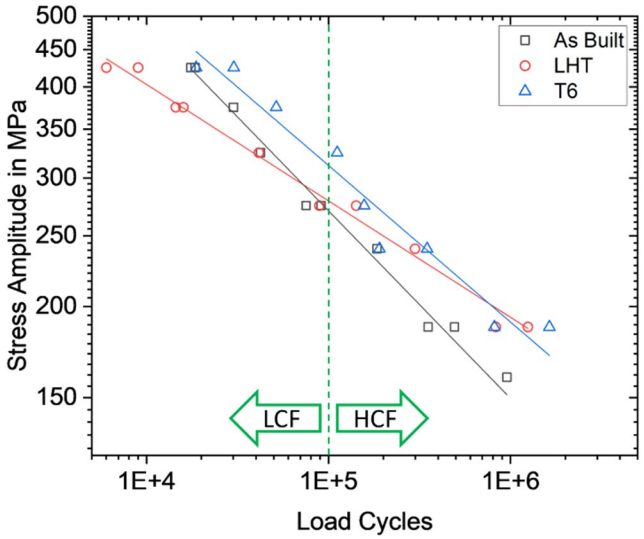

Fig. 13 S-N curves for as-built, LHT and T6 heat-treated specimens in the high cycle fatigue region between 1E4 and 1E6 load cycles. Load cycle numbers < 1E5 are considered as the low cycle fatigue (LCF) regime. Load cycle numbers > 1E5 are considered as the high cycle fatigue (HCF) regime [59]

absorption [24]. The fracture of the T6 specimens shows numerous pores and Si-particles in the fracture surface (see Fig. 12h&i). Recently published investigations show that Si-particles and pores in T6 heat treated AlSi10Mg can facilitate crack propagation during fracture [19, 58].

Investigations of the fatigue behavior were performed with 3-point-bending tests and a stress ratio of $R = -1$. Resulting S-N curves (Woehler curves) are presented in Fig. 13. The S-N curves were calculated for a failure probability of 50%. The stress amplitude refers to the calculated fictional stress on the surface of the specimen based on geometry and selected torque. The true stress is presumably lower due to plastic deformation.

For high stress amplitudes (325–425 MPa) the T6 heat-treated specimens perform best while the LHT specimens reach the fewest load cycles until failure. The S-N curve of the as-built specimens possesses the steepest gradient leading to the curve cross with the S-N curve of the LHT specimen. Consequently, as-built specimens reach the fewest load cycles when experiencing low stress amplitudes (187.5–240 MPa). Due to the low gradient of the S-N curve the LHT specimens are on a par with the T6 heat treated specimens in the lower stress region.

Fatigue behavior is strongly influenced by the residual stress in the tested parts [60]. Figure 14a shows results from residual stress measurements performed on the polished surface of the specimens. The as-built specimen shows a residual tensile stress of 37.8 MPa in build direction. Investigations on residual stress presented in literature report residual tensile stress values of 99–115 MPa [21, 26] for surfaces of as-built specimens. It is assumed that the additional polishing process in this study reduced the surface residual stress as demonstrated by Di Egidio et al. and Lehner et al. [26, 61]. As shown in Sect. 3.1 the microstructure and hardness after LHT are comparable to that of parts after a stress relief heat treatment. Lehner et al. [21] reported no significant residual stress remaining at the specimens surface after a conventional stress relief heat treatment at 300 °C for 2 h. However, the present investigation shows residual compressive stress of − 25.0 MPa at the surface of the LHT specimen. This additional compressive stress is most likely induced by the grinding and polishing after LHT. The homogeneous heating and slow cooling of the specimen

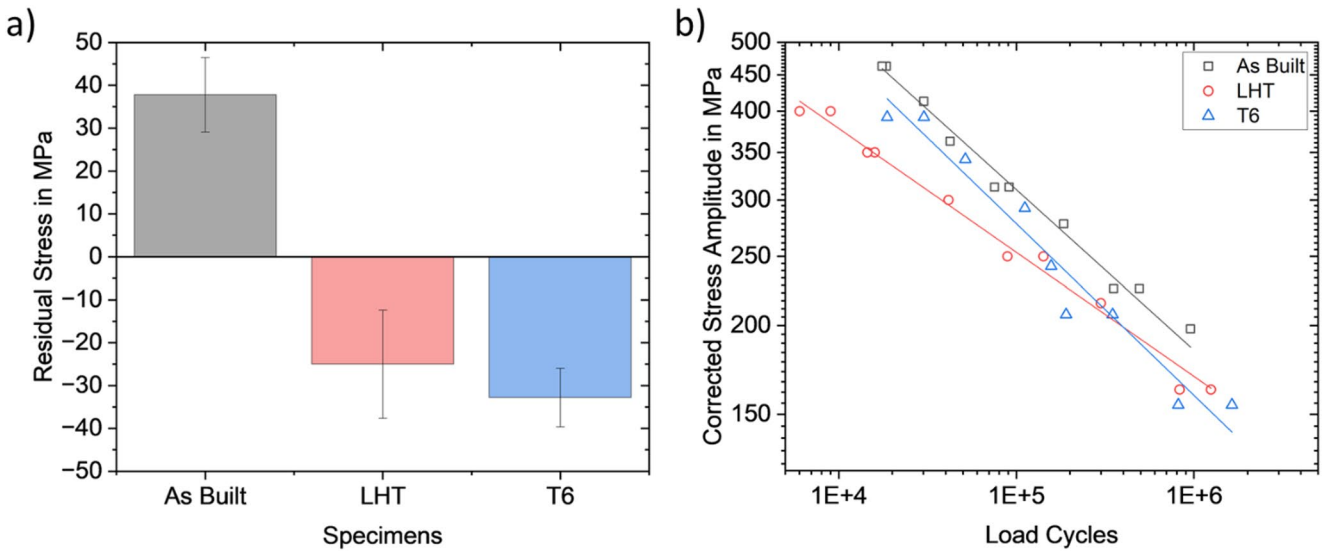

Fig. 14 **a** Residual stress in build direction for all materials, measured at the polished surface of the fatigue specimens. **b** S-N curves corrected by superimposing the measured residual stress

during LHT makes it unlikely for thermal residual stresses to arise. The T6 heat-treated specimens also show residual compressive stress (-32.8 MPa) at the surface which is in good agreement with values reported by [21]. The residual compressive stress is most likely induced during quenching after the solution heat treatment [62] and not relieved by the subsequent artificial aging. Figure 14b shows the S-N curves with the stress amplitudes corrected by the measured residual stress values. Including the residual stress emphasizes that the as-built specimens endure the highest stress amplitude.

The surface quality is equally good for all three specimen types with Ra-values of 0.36 µm (as-built), 0.22 µm (LHT) and 0.19 µm (T6). The EBSD investigation showed no alteration of the grain structure (see Fig. 10j-l) by the heat treatments. Therefore, the gradient of the S-N curves is presumably influenced by the ductility of the material and the crack propagation mechanism.

The as-built specimens possess a high tensile strength but low ductility and therefore a more brittle material behavior. As seen in Fig. 12c, the crack propagation for the as-built specimen occurs along the Si-rich network. The additional residual tensile stress effectively increases the total stress straining the material at the surface thereby facilitating crack initiation and crack propagation and ultimately decreases the fatigue strength. The resulting steep gradient of the S-N curve for as-built specimen compared to T6 specimen (Fig. 13) is in good agreement with the observations of Aboulkhair et al. [25]. The maximum applied stress amplitude is approximately equal to the measured UTS of the as-built specimens.

The LHT and T6-heat-treated specimens possess a considerably lower tensile strength compared to the as-built condition but a significantly increased ductility. For ductile materials the fatigue behavior can be separated into the low cycle fatigue regime (LCF, $N < 1E5$) and the high cycle fatigue regime (HCF, $N = 1E5 \ldots 1E7$) [59]. The fatigue behavior in the LCF regime is primarily governed by the crack propagation, which is determined by the plastic material behavior [59]. In the HCF regime the elastic material properties and the crack initiation are decisive for the fatigue performance [59].

Compared to the as-built condition, the T6 heat treatment improves the fatigue behavior in the LCF and HCF regime due to the homogeneous microstructure and the induced residual compressive stress [25, 26]. The disintegration of the Si-network and the dissolution of the heterogeneous scan track structure (see Fig. 10c) hinder the crack propagation [31]. Moreover, the T6-heat-treated condition is known for a high potential for cyclic hardening, further improving the crack propagation resistance [61]. In the HCF the fatigue performance of T6-heat-treated specimens is most likely determined by premature crack initiation at pore defects developed during the T6 heat treatment process. Similar fatigue performance results for T6 heat-treated specimens were achieved by Lehner et al. [61].

For the LHT specimens, the crack propagation is most likely hampered by the more homogeneous microstructure. The higher ductility caused by the disintegration of the Si-network presumably leads to plastic deformations and crack closure phenomena at the crack tip, as observed by Roveda et al. [30] for the stress-relieved parts with similar microstructure and mechanical properties. Despite a tensile strength and ductility comparable to the T6 specimens, the LHT specimens perform poorly in the LCF regime at high stress amplitudes. This could be attributed to the crack closure phenomenon being less relevant at high stress amplitudes [61]. Furthermore, Lehner et al. [21] report a lack of cyclic hardening for stress-relieved PBF-LB parts, which possess a similar microstructure and tensile properties as LHT parts. The lack of cyclic hardening compared to the T6-heat-treated condition in combination with the reduced UTS compared to the as-built condition leads to the observed low fatigue strength in the LCF regime. However, due to the higher defect tolerance evoked by the high ductility [21] and the absence of pore defects, the fatigue performance in the HCF regime is better than for as-built specimens and equal to the T6-heat-treated specimens due to a delayed crack initiation, which leads to the observed low gradient of the S-N curve for LHT specimens.

Figure 15 shows SEM images of fracture surfaces, which were all taken from specimens tested with a stress amplitude of 275 MPa. There are crack initiations on the top and the bottom surface which is expected due to the alternating load direction. Most cracks are initiated by surface defects and not by pore defects. This can be attributed to the grinding and polishing of the surface which effectively closes pores at the surface. The smooth fatigue fracture surface caused by stable crack propagation is highlighted with dashed, yellow lines and is larger for the as-built and LHT specimen compared to the T6 heat-treated specimen. The larger residual fracture area of the T6 heat-treated specimen hints at a premature failure, possibly caused by stress concentrations around pores. This possibly contributes to a steeper S-N curve compared to the LHT specimen and thereby equal or lower fatigue strength for load cycle numbers > 1E6.

4 Discussion

The microstructural investigation showed a continuous breakdown of the Si-rich network structure and agglomeration of Si in particles along the cell boundaries with Si-particle size increasing with the heat input. This is accompanied

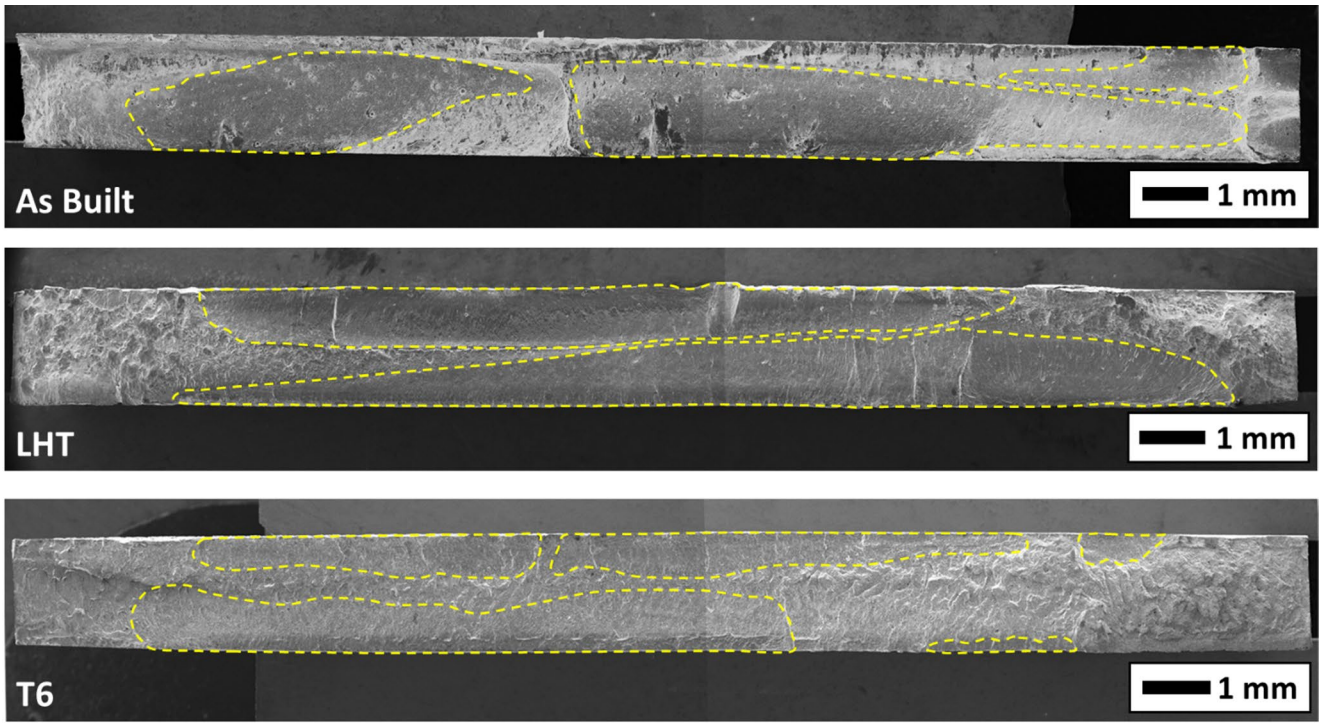

Fig. 15 SEM images of fatigue fracture surfaces. Presented specimens were tested at a stress amplitude of 275 MPa. Regions of stable crack propagation are highlighted with yellow dashed lines

by the precipitation of nano-sized Si-particles in the supersaturated α-Al phase. This leads to a reduction in hardness which correlates with the increasing particle size. The strength of PBF-LB manufactured AlSi10Mg parts however stems from the intact cell boundaries, which impede the dislocation movement between cells [13, 14]. This is demonstrated by the rapid loss in hardness coinciding with small Si-particles at the beginning of the disintegration of the Si-rich network. The regression analysis applied to the LHT process parameters shows, that the described mechanism is mainly governed by the process parameters laser power P and the feed rate v. Moreover, the part geometry and the different thermal mass coming with it influence the resulting hardness in the processing area and most of all the spatial effect of the LHT around the process area. The investigation shows that based on the described microstructural mechanism a local and continuous adjustment of the hardness from the as-built condition (125 HV) down to around 80 HV is possible.

The investigation of the tensile properties shows that, despite a significantly lower hardness, both the UTS and the ductility of LHT parts, is slightly higher than those of the T6-heat-treated specimens. This represents a breach of the strength-ductility trade-off [63], which can be primarily attributed to the pore formation during T6 heat treatment, reducing strength and ductility compared to LHT. Despite exceeding the temperature threshold of 500 °C for pore formation during heat treatment [64], no pore defects were detected for the LHT process. The measurement of the superficial residual stress proves that the LHT effectively eliminates tensile residual stress. The fatigue performance of the tested LHT specimens is only preferable in the HCF regime with stress amplitudes below the materials UTS and therefore high load cycle numbers. This may be especially beneficial for applications involving vibrational loading, for example in the aerospace sector. The fatigue performance is most likely determined by an increased defect tolerance and delayed crack initiation when compared to the T6 and as-built condition as well as the crack closure phenomena, which was reported for similar microstructures [30]. The low fatigue strength in the LCF regime can be explained by the lack of cyclic hardening, which is more pronounced for the as-built and especially T6 condition. Future research with a spectrum of LHT material conditions is needed to assess the competing effects which define the fatigue properties and determine the optimal microstructural state to improve fatigue performance also in the LCF regime.

The microstructure and mechanical properties of LHT parts are similar to those of conventionally stress-relieved PBF-LB manufactured parts. While Lehner et al. [21] concluded that the fatigue performance of stress-relieved and as-built parts is primarily determined by pore defects and defect tolerance, the present investigation on LHT shows crack initiation on superficial defects. This discrepancy is

most likely due to the small specimen size compared to Lehner et al., as it is known, that with increasing part size the probability of macroscopic pore defects critical to failure rises [21]. The results for the microstructure and mechanical properties of T6 heat-treated parts are in good agreement with other reports in literature [23, 61]. The worsening of fatigue properties due to T6 heat treatment as reported by Baek et al. [28] was not confirmed.

In the present study the selected specimen geometry is a rectangular solid. This is suitable for investigation of the underlying mechanisms of microstructural changes and the manufacturing of mechanical testing specimens However, PBF-LB manufactured parts for real-life applications often have complex shapes [65], so that a transition to an industrialized process is necessary. The implementation of the LHT process for complex part geometries can be achieved with scanner optics and robot kinematics as is already implemented for remote laser welding processes [66, 67]. Based on the presented results, in future works a thermal simulation of the three-dimensional temperature field in complex parts as well as a kinetic simulation of the Si-diffusion could be developed to predict the resulting microstructure.

5 Conclusion

The present study focuses on the microstructure modification of AlSi10Mg PBF-LB manufactured parts by means of laser heat treatment (LHT). The LHT enables to locally adjust the material hardness between the as-built condition (125.6 HV) and a minimum of around 80 HV. The hardness reduces more when increasing the heat input either by increasing the laser power or decreasing the feed rate. The part geometry significantly impacts the hardness resulting after LHT due to the individual conditions of heat flow and dissipation resulting in different temperature gradients. The change in hardness is primarily determined by breaking up the Si-rich network and subsequent agglomeration of Si-particles. Microstructure and hardness after LHT are similar to that of parts treated with a conventional stress relief heat treatment.

Investigations of the mechanical properties show that LHT decreases the ultimate tensile strength (273 MPa) compared to the as-built condition (422 MPa). However, UTS and ductility are slightly higher compared to T6 heat-treated specimens. In the LCF regime, at stress amplitudes above the UTS of the LHT specimens, the fatigue strength of the LHT specimens is the lowest compared to the as-built and T6 heat treated specimens. For stress amplitudes lower than the UTS the fatigue strength of the LHT specimens is above the fatigue strength of the as-built specimens and on a par with the T6 heat-treated specimens. Regarding the mechanical properties, results show that, LHT could in some applications be a viable alternative for a conventional T6 heat treatment. Moreover, LHT allows to adjust the microstructure and mechanical properties in a wide range and also restricts the effect to the desired part area. It is therefore a promising option to locally tailor mechanical properties of PBF-LB manufactured parts to the applications requirements.

Appendix

Appendix A1: summary of all tested process parameters and resulting hardness

Table 3 Summary of all tested parameter combinations. Maximum temperature (T_{max}) and heating time over 200 °C (t) are taken from exemplary pyrometer measurements. Hardness values represent the mean hardness value in the center of the specimen corresponding to the temperature measurement. Results of parameter combinations marked with an asterisk are discussed in Figs. 3, 4 and 6.

No.	Laser Power in W	Feed Rate in m/min	Laser Beam Diameter in mm	T_{max} in °C	t (T>200 °C) in s	Hardness HV 0.1
1*	320	0.25	7.5	365.5	28.87	115.1±2.66
2*	350	0.25	7.5	378.4	37.48	108.8±5.21
3*	380	0.25	7.5	406.2	43.42	106.7±4.15
4*	440	0.25	7.5	455.7	51.04	96.4±2.73
5*	500	0.25	7.5	557.3	65.11	84±1.10
6*	320	0.2	7.5	405.0	45.74	104.5±4.63
7	350	0.2	7.5	486.7	58.79	92.5±2.83
8	380	0.2	7.5	460.1	56.14	94.7±1.45
9	440	0.2	7.5	516.6	61.82	82.2±1.68
10*	320	0.15	7.5	470.4	67.43	84.6±2.13
11	320	0.25	10	335.5	32.79	113.5±4.04
12*	320	0.2	10	339.3	42.70	106.9±4.65
13	320	0.15	10	413.6	60.56	94.6±1.15
14*	320	0.2	5	442.5	42.42	102.5±2.93
15	240	0.3333	5.625	284.8	1.39	119.2±4.79
16	160	0.5	3.75	325.9	0.54	125.6±3.67
17	330	0.3333	5.625	357.3	17.18	116.5±3.68
18	220	0.5	3.75	380.0	0.71	121.7±4.49

Appendix A2: weighted least square (WLS) linear regression model

Equation of the used WLS linear regression model:

$$H = \beta_0 + \beta_P\left(P - \bar{P}\right) + \beta_v\left(v - \bar{v}\right) + \beta_d\left(d - \bar{d}\right) + \beta_{Pv}\left(P - \bar{P}\right)\left(v - \bar{v}\right) + \beta_{Pd}\left(P - \bar{P}\right)\left(d - \bar{d}\right) + \beta_{vd}\left(v - \bar{v}\right)\left(d - \bar{d}\right) \quad (3)$$

Table 4 Summary of the complete results of the WLS regression analysis

	Coefficient	Std.Err.	t	*p*	[0.025	0.975]
β	110.61	2.07	53.41	1.2E-14	106.05	115.17
β_P	− 0.13	0.02	− 7.69	9.5E-06	− 0.17	− 0.10
β_v	196.25	27.58	7.11	2.0E-05	135.54	256.95
β_d	2.50	1.61	1.55	0.15	− 1.05	6.05
β_{Pv}	− 0.03	0.49	− 0.06	0.96	− 1.10	1.05
β_{Pd}	− 0.05	0.05	− 1.19	0.26	− 0.16	0.05
β_{vd}	22.26	12.42	1.79	0.10	− 5.07	49.58

Acknowledgements The presented work was funded by the Ministry of Science, Research and the Arts of the Federal State of Baden-Wuerttemberg within the 'InnovationCampus Future Mobility', which is gratefully acknowledged.

Author contributions Conceptualization: SK, MJ, TG, VS & FZ; Methodology: SK, MJ; Formal analysis: SK; Investigation: SK; Visualization: SK; Resources: TG, VS & FZ; Funding Acquisition: MJ; Project administration: MJ; Supervision: MJ, TG & VS; Writing – original draft: SK; Writing – review & editing: MJ, TG, VS & FZ.

Funding Open Access funding enabled and organized by Projekt DEAL.

Data availability All data supporting the findings of this study are available within the paper and its Supplementary Information.

Declarations

Conflict of interest For this research, there is no conflict of interest for all authors.

References

1. Yan Q, Song B, Shi Y (2020) Comparative study of performance comparison of AlSi10Mg alloy prepared by selective laser melting and casting. J Mater Sci Technol 41:199–208. https://doi.org/10.1016/j.jmst.2019.08.049
2. Girelli L, Tocci M, Montesano L et al (2017) Optimization of heat treatment parameters for additive manufacturing and gravity casting AlSi10Mg alloy. IOP Conf Ser : Mater Sci Eng 264:12016. https://doi.org/10.1088/1757-899X/264/1/012016
3. Li W, Li S, Liu J et al (2016) Effect of heat treatment on AlSi10Mg alloy fabricated by selective laser melting: Microstructure evolution, mechanical properties and fracture mechanism. Mater Sci Engineering: A 663:116–125. https://doi.org/10.1016/j.msea.2016.03.088
4. Nicoletto G, Gallina L, Riva E (2019) Influence of as-built surfaces on the fatigue behavior of AlSi10Mg parts obtained by laser powder bed fusion. Procedia Struct Integr 24:381–389. https://doi.org/10.1016/j.prostr.2020.02.035
5. Read N, Wang W, Essa K et al (2015) Selective laser melting of AlSi10Mg alloy: Process optimisation and mechanical properties development. Mater Des (1980–2015) 65:417–424. https://doi.org/10.1016/j.matdes.2014.09.044
6. Kempen K, Thijs L, van Humbeeck J et al (2012) Mechanical Properties of AlSi10Mg Produced by Selective Laser Melting. Physics Procedia 39:439–446. https://doi.org/10.1016/j.phpro.2012.10.059
7. Kumar Ramavajjala A, Dandekar TR, Khatirkar RK et al (2025) A review on the correlation between microstructure, heat treatment and mechanical properties of additively manufactured AlSi10Mg by LPBF. Crit Rev Solid State Mater Sci 50:239–274. https://doi.org/10.1080/10408436.2024.2414012
8. Trevisan F, Calignano F, Lorusso M et al (2017) On the Selective Laser Melting (SLM) of the AlSi10Mg Alloy: Process, Microstructure, and Mechanical Properties. Mater (Basel) 10. https://doi.org/10.3390/ma10010076
9. Neuser M, Grydin O, Frolov Y et al (2022) Influence of solidification rates and heat treatment on the mechanical performance and joinability of the cast aluminium alloy AlSi10Mg. Prod Eng Res Devel 16:193–202. https://doi.org/10.1007/s11740-022-01106-1
10. Sathishkumar A, Soundararajan R, Sivasankaran S (2022) Effect of Direct Aging on the Microstructure and Mechanical Behavior of AlSi10Mg Alloy: Casting Versus Selective Laser Melting. J Materi Eng Perform 32:3215–3229. https://doi.org/10.1007/s11665-022-07315-0
11. Hyer H, Le Zhou, Park S et al (2020) Understanding the Laser Powder Bed Fusion of AlSi10Mg Alloy. Metallogr Microstruct Anal 9:484–502. https://doi.org/10.1007/s13632-020-00659-w
12. Wu J, Wang XQ, Wang W et al (2016) Microstructure and strength of selectively laser melted AlSi10Mg. Acta Mater 117:311–320. https://doi.org/10.1016/j.actamat.2016.07.012
13. Kwon J, Choi YT, Kim ES et al (2024) Effect of cell characteristics on mechanical properties of AlSi10Mg alloy fabricated by laser powder bed fusion. Mater Sci Engineering: A 901:146537. https://doi.org/10.1016/j.msea.2024.146537
14. Chen B, Moon SK, Yao X et al (2017) Strength and strain hardening of a selective laser melted AlSi10Mg alloy. Scripta Mater 141:45–49. https://doi.org/10.1016/j.scriptamat.2017.07.025
15. Chmelko V, Šulko M, Škriniarová J et al (2023) Strength and Cyclic Properties of Additive vs. Conventionally Produced Mater AlSi10Mg Mater (Basel) 16. https://doi.org/10.3390/ma16072598
16. Fiocchi J, Tuissi A, Biffi CA (2021) Heat treatment of aluminium alloys produced by laser powder bed fusion: A review. Mater Design:109651. https://doi.org/10.1016/j.matdes.2021.109651
17. Brandl E, Heckenberger U, Holzinger V et al (2012) Additive manufactured AlSi10Mg samples using Selective Laser Melting (SLM): Microstructure, high cycle fatigue, and fracture behavior. Mater Design 34:159–169. https://doi.org/10.1016/j.matdes.2011.07.067

18. Cabrini M, Lorenzi S, Testa C et al (2021) Effect of Heat Treatment on Microstructure and Selective Corrosion of LPBF-AlSi10Mg by Means of SKPFM and Exo-Electron Emission. Mater (Basel) 14. https://doi.org/10.3390/ma14195602
19. Baig S, Ghiaasiaan R, Shao S et al (2023) Tensile and fatigue behaviors of additively manufactured AlSi10Mg: Effect of solutionizing and aging heat treatments. Fatigue Fract Eng Mat Struct 46:2662–2680. https://doi.org/10.1111/ffe.14024
20. Aboulkhair NT, Maskery I, Tuck C et al (2016) The microstructure and mechanical properties of selectively laser melted AlSi10Mg: The effect of a conventional T6-like heat treatment. Mater Sci Engineering: A 667:139–146. https://doi.org/10.1016/j.msea.2016.04.092
21. Lehner P, Blinn B, Beck T (2023) Improving the Defect Tolerance and Fatigue Strength of AM AlSi10Mg. Adv Eng Mater 25(15):2201855. https://doi.org/10.1002/adem.202201855
22. Mfusi BJ, Mathe NR, Motibane L et al (2025) The effect of T6 and hot isostatic pressure thermal treatments on the crack fatigue growth and fracture toughness of AlSi10Mg produced by additive manufacturing. J Manuf Process 151:1042–1057. https://doi.org/10.1016/j.jmapro.2025.07.065
23. Sajadi F, Tiemann J-M, Bandari N et al (2021) Fatigue Improvement of AlSi10Mg Fabricated by Laser-Based Powder Bed Fusion through Heat Treatment. Metals 11:683. https://doi.org/10.3390/met11050683
24. Padovano E, Badini C, Pantarelli A et al (2020) A comparative study of the effects of thermal treatments on AlSi10Mg produced by laser powder bed fusion. J Alloys Compd 831:154822. https://doi.org/10.1016/j.jallcom.2020.154822
25. Aboulkhair NT, Maskery I, Tuck C et al (2016) Improving the fatigue behaviour of a selectively laser melted aluminium alloy: Influence of heat treatment and surface quality. Mater Design 104:174–182. https://doi.org/10.1016/j.matdes.2016.05.041
26. Di Egidio G, Ceschini L, Morri A et al (2023) Room- and High-Temperature Fatigue Strength of the T5 and Rapid T6 Heat-Treated AlSi10Mg Alloy Produced by Laser-Based Powder Bed Fusion. Metals 13:263. https://doi.org/10.3390/met13020263
27. Di Egidio G, Tonelli L, Zanni M et al (2024) Direct artificial aging of the PBF-LB AlSi10Mg alloy designed to enhance the trade-off between strength and residual stress relief. J Alloys Metall Syst 5:100063. https://doi.org/10.1016/j.jalmes.2024.100063
28. Baek M-S, Kreethi R, Park T-H et al (2021) Influence of heat treatment on the high-cycle fatigue properties and fatigue damage mechanism of selective laser melted AlSi10Mg alloy. Mater Sci Engineering: A 819:141486. https://doi.org/10.1016/j.msea.2021.141486
29. Marola S, Bosia S, Veltro A et al (2021) Residual stresses in additively manufactured AlSi10Mg: Raman spectroscopy and X-ray diffraction analysis. Mater Design 202:109550. https://doi.org/10.1016/j.matdes.2021.109550
30. Roveda I, Serrano-Munoz I, Haubrich J et al (2023) Influence of post-process heat treatments on the fatigue crack propagation behaviour of a PBF-LB/M AlSi10Mg alloy. Int J Fatigue 175:107808. https://doi.org/10.1016/j.ijfatigue.2023.107808
31. Fernandes RF, Jesus JS, Branco R et al (2025) Effect of low-temperature stress relieving heat treatments on fatigue behaviour and failure mechanisms of L-PBF AlSi10Mg aluminium alloy. Eng Fail Anal 169:109210. https://doi.org/10.1016/j.engfailanal.2024.109210
32. van Cauwenbergh P, Samaee V, Thijs L et al (2021) Unravelling the multi-scale structure-property relationship of laser powder bed fusion processed and heat-treated AlSi10Mg. Sci Rep 11:6423. https://doi.org/10.1038/s41598-021-85047-2
33. Takata N, Kodaira H, Sekizawa K et al (2017) Change in microstructure of selectively laser melted AlSi10Mg alloy with heat treatments. Mater Sci Engineering: A 704:218–228. https://doi.org/10.1016/j.msea.2017.08.029
34. Hwang WJ, Bang GB, Choa S-H (2023) Effect of a Stress Relief Heat Treatment of AlSi7Mg and AlSi10Mg Alloys on Mechanical and Electrical Properties According to Silicon Precipitation. Met Mater Int 29:1311–1322. https://doi.org/10.1007/s12540-022-01304-7
35. Li Z, Li Z, Tan Z et al (2020) Stress relaxation and the cellular structure-dependence of plastic deformation in additively manufactured AlSi10Mg alloys. Int J Plast 127:102640. https://doi.org/10.1016/j.ijplas.2019.12.003
36. Roveda I, Serrano-Munoz I, Haubrich J et al (2024) Investigation on the fatigue strength of AlSi10Mg fabricated by PBF-LB/M and subjected to low temperature heat treatments. Mater Design 244:113170. https://doi.org/10.1016/j.matdes.2024.113170
37. Valim DB, Ávila JA, Fonseca EB et al (2024) Influence of build orientation and heat treatment on high cycle fatigue of additively manufactured AlSi10Mg. Mater Sci Engineering: A 916:147308. https://doi.org/10.1016/j.msea.2024.147308
38. Tang H, Gao C, Zhang Y et al (2023) Effects of direct aging treatment on microstructure, mechanical properties and residual stress of selective laser melted AlSi10Mg alloy. J Mater Sci Technol 139:198–209. https://doi.org/10.1016/j.jmst.2022.08.032
39. Park T-H, Baek M-S, Hyer H et al (2021) Effect of direct aging on the microstructure and tensile properties of AlSi10Mg alloy manufactured by selective laser melting process. Mater Charact 176:111113. https://doi.org/10.1016/j.matchar.2021.111113
40. Fousová M, Dvorský D, Michalcová A et al (2018) Changes in the microstructure and mechanical properties of additively manufactured AlSi10Mg alloy after exposure to elevated temperatures. Mater Charact 137:119–126. https://doi.org/10.1016/j.matchar.2018.01.028
41. Fite J, Eswarappa Prameela S, Slotwinski JA et al (2020) Evolution of the microstructure and mechanical properties of additively manufactured AlSi10Mg during room temperature holds and low temperature aging. Additive Manuf 36:101429. https://doi.org/10.1016/j.addma.2020.101429
42. Qi X, Liang X, Wang J et al (2024) Microstructure tailoring in laser powder bed fusion (L-PBF): Strategies, challenges, and future outlooks. J Alloys Compd 970:172564. https://doi.org/10.1016/j.jallcom.2023.172564
43. Leis A, Traunecker D, Weber R et al (2022) Tuning the Hardness of Produced Parts by Adjusting the Cooling Rate during Laser-Based Powder Bed Fusion of AlSi10Mg by Adapting the Process Parameters. Metals 12:2000. https://doi.org/10.3390/met12122000
44. Noell PJ, Rodelas JM, Ghanbari ZN et al (2020) Microstructural modification of additively manufactured metals by electropulsing. Additive Manuf 33:101128. https://doi.org/10.1016/j.addma.2020.101128
45. Moradi M, Arabi H, Jamshidi Nasab S et al (2019) A comparative study of laser surface hardening of AISI 410 and 420 martensitic stainless steels by using diode laser. Opt Laser Technol 111:347–357. https://doi.org/10.1016/j.optlastec.2018.10.013
46. Ours B, Rehman HU, Downard S et al (2025) Localized Laser Heat Treatment on AISI 1045 Steel Using a LPBF Laser. Eng Rep 7(1):e13045. https://doi.org/10.1002/eng2.13045
47. Merklein M, Geiger M (2002) New materials and production technologies for innovativ lightweight constructions. J Mater Process Technol 125:532–536
48. Maier V, Hausöl T, Schmidt CW et al (2012) Tailored Heat Treated Accumulative Roll Bonded Aluminum Blanks: Microstructure and Mechanical Behavior. Metall Mater Trans A 43:3097–3107. https://doi.org/10.1007/s11661-012-1151-3
49. Merklein M, Böhm W, Lechner M (2012) Tailoring Material Properties of Aluminum by Local Laser Heat

Treatment. Physics Procedia 39:232–239. https://doi.org/10.1016/j.phpro.2012.10.034
50. Mohammadi A, Vanhove H, van Bael A et al (2012) Bending Properties of Locally Laser Heat Treated AA2024-T3 Aluminium Alloy. Physics Procedia 39:257–264. https://doi.org/10.1016/j.phpro.2012.10.037
51. Kramer S, Jarwitz M, Schulze V et al (2024) Local laser heat treatment of AlSi10Mg as-built parts produced by Laser Powder Bed Fusion. Procedia CIRP 124:74–77. https://doi.org/10.1016/j.procir.2024.08.074
52. Leis A, Weber R, Graf T (2020) Influence of the process parameters on the absorptance during Laser-Based Powder Bed Fusion of AlSi10Mg. Procedia CIRP 94:173–176. https://doi.org/10.1016/j.procir.2020.09.033
53. Yaru L, Tiejun M, Tounan J et al (2023) Aging temperature effects on microstructure and mechanical properties for additively manufactured AlSi10Mg. Mater Sci Technol 39:1223–1236. https://doi.org/10.1080/02670836.2022.2164128
54. Ogris E, Wahlen A, Lüchinger H et al (2002) On the silicon spheroidization in Al–Si alloys. J Light Met 2:263–269. https://doi.org/10.1016/S1471-5317(03)00010-5
55. Beevers E, Brandão AD, Gumpinger J et al (2018) Fatigue properties and material characteristics of additively manufactured AlSi10Mg – Effect of the contour parameter on the microstructure, density, residual stress, roughness and mechanical properties. Int J Fatigue 117:148–162. https://doi.org/10.1016/j.ijfatigue.2018.08.023
56. Girelli L, Tocci M, Gelfi M et al (2019) Study of heat treatment parameters for additively manufactured AlSi10Mg in comparison with corresponding cast alloy. Mater Sci Engineering: A 739:317–328. https://doi.org/10.1016/j.msea.2018.10.026
57. Ghio E, Cerri E (2022) Additive Manufacturing of AlSi10Mg and Ti6Al4V Lightweight Alloys via Laser Powder Bed Fusion: A Review of Heat Treatments Effects. Mater (Basel) 15. https://doi.org/10.3390/ma15062047
58. Di Egidio G, Ceschini L, Morri A et al (2022) A Novel T6 Rapid Heat Treatment for AlSi10Mg Alloy Produced by Laser-Based Powder Bed Fusion: Comparison with T5 and Conventional T6 Heat Treatments. Metall Mater Trans B 53:284–303. https://doi.org/10.1007/s11663-021-02365-6
59. Mughrabi H (2015) Microstructural mechanisms of cyclic deformation, fatigue crack initiation and early crack growth. Philos Trans Math Phys Eng Sci 373(2038). https://doi.org/10.1098/rsta.2014.0132
60. Maleki E, Bagherifard S, Guagliano M (2023) Correlation of residual stress, hardness and surface roughness with crack initiation and fatigue strength of surface treated additive manufactured AlSi10Mg: Experimental and machine learning approaches. J Mater Res Technol 24:3265–3283. https://doi.org/10.1016/j.jmrt.2023.03.193
61. Lehner P, Blinn B, Zhu T et al (2024) Influence of the as-built surface and a T6 heat treatment on the fatigue behavior of additively manufactured AlSi10Mg. Int J Fatigue 187:108479. https://doi.org/10.1016/j.ijfatigue.2024.108479
62. Kim I, Park SC, Kim YI et al (2023) Surface residual stress analysis of additive manufactured AlSi10Mg alloys. J Alloys Compd 945:169315. https://doi.org/10.1016/j.jallcom.2023.169315
63. Dang B, Zhang X, Chen YZ et al (2016) Breaking through the strength-ductility trade-off dilemma in an Al-Si-based casting alloy. Sci Rep 6:30874. https://doi.org/10.1038/srep30874
64. Strumza E, Hayun S, Barzilai S et al (2019) In situ detection of thermally induced porosity in additively manufactured and sintered objects. J Mater Sci 54:8665–8674. https://doi.org/10.1007/s10853-019-03452-5
65. Uriati F, Zambrelli L, Nicoletto G et al (2021) Design, production, and fatigue testing of an optimized structural component made of L-PBF AlSi10Mg. Procedia Struct Integr 34:184–190. https://doi.org/10.1016/j.prostr.2021.12.027
66. Ceglarek D, Colledani M, Váncza J et al (2015) Rapid deployment of remote laser welding processes in automotive assembly systems. CIRP Ann 64:389–394. https://doi.org/10.1016/j.cirp.2015.04.119
67. Fysikopoulos A, Pastras G, Stavridis J et al (2016) On the Performance Evaluation of Remote Laser Welding Process: An Automotive Case Study. Procedia CIRP 41:969–974. https://doi.org/10.1016/j.procir.2016.01.005